TÉCNICO LISBOA

MULTIPHYSICS SIMULATION OF PV MODULES

Pankaj Arora

Thesis to obtain the Master of Science Degree in

Energy Engineering and Management

Supervisors: M.Sc. Matthieu Ebert

Prof. Susana Isabel Pinheiro Cardoso de Freitas

Examination Committee

Chaiperson: Prof. Luís Filipe Moreira Mendes

Supervisor: Prof. Susana Isabel Pinheiro Cardoso de Freitas

Member of the Committee: Dr. Vânia Cristina Henriques Silvério

October 2016

ABSTRACT

Modeling and simulation of Photovoltaic (PV) modules play an important role for the development of the technology and evaluation of new designs. A Finite Element Method (FEM) based multiphysics simulation software package is used in this work to study and analyze optical, thermal and electrical behavior of PV modules. An increase in transmittance by 10-15% at low elevation angles and reduction in busbar/ribbon shadow loss by almost 3% of cell irradiance is calculated from optical simulations of structured glass models. To determine the temperature distribution in a PV module, a novel thermal model based on the optical properties of module components is presented. Electrical (ohmic) loss in the emitter for homogeneous and inhomogeneous cell illumination is studied. Using coupled optical and electrical simulations, performance of grid models is investigated. Validation of the multiphysics study comprising of ray-tracing and heat transfer tools is done by outdoor experiments. Experiment and simulation results lay within an average absolute temperature difference of $0.6 \pm 2^{o}C$ for three different illumination cases investigated.

Keywords- Photovoltaic (PV) modules; Finite Element Method; Multiphysics Simulation; Structured glass

---

RESUMO

A modelação e simulação de módulos fotovoltaicos são etapas importantes no desenvolvimento de tecnologias e qualificação de novos desenhos. Nesta tese aplicamos códigos de simulação baseados em métodos de elementos finitos para estudar e analizar as caracteristicas ópticas, térmicas e eléctricas de módulos fotovoltaicos. De acordo com os cálculos realizados com modelos baseados em vidro estruturado, é possível obter aumentos de transmitância na ordem de 10-15% em baixos ângulos e diminuição do efeito de sombra em quase 3% da célula. Apresentamos um modelo inovador para a distribuição de temperatura no módulo fotovoltaico, baseado nas propriedades ópticas dos componentes do módulo. Os efeitos dissipativos por condução de corrente eléctrica (perdas resistivas) são considerados no modelo, para perfis de iluminação homogénea e inhomogénea. Neste trabalho investigamos o desempenho dos modelos em rede, acoplando simulações ópticas e eléctricas. Finalmente, a validação dos modelos baseados em raios de luz e transferência de calor é feita com experiências no exterior. Os resultados experimentais estão concordantes com as simulações, indicando diferenças de temperatura de $0.6 \pm 2^{o}C$, para as três situações estudadas.

Palavras-Chave- Módulos fotovoltaicos; Método de elementos finitos; Simulação Multiphysics; vidro estruturado

CONTENTS

NOMENCLATURE

Symbol	Definition	Unit
α	Absorption coefficient	1/m
β	Volumetric temperature coefficient	1/K
ε	Emissivity	-
σ	Stefan-Boltzmann constant	$W/(m^2K^4)$
σ_{sd}	Standard deviation	m
ρ	Volumetric mass density	kg/m^3
ρ_e	Emitter sheet resistivity	Ω/square
λ	Wavelength	m
η_c	Cell efficiency	-
η_{ref}	Efficiency at reference temperature	-
θ_i	Angle of incidence	degree
θ_r	Angle of reflection	degree
θ_t	Angle of refraction	degree
∇T	Temperature gradient	K/m
ΔT	Temperature difference	K
c	Speed of light in medium	m/s
c_0	Speed of light in vacuum	m/s
C_p	Specific heat capacity	J/(kg K)
d	Distance travelled by light ray	m
d_f	Distance between alternate fingers	m
ds	Differential length element	m
h	Convective heat-transfer coefficient	$W/(m^2K)$
I	Current	A
I_{irr}	Irradiance intensity	W/m^2
I_0	Incident light intensity	W/m^2
I_m	Maximum power point current	A
I_{peak}	Peak Irradiance intensity of distribution	W/m^2
I_{ph}	Photocurrent	A
I_s	Diode saturation current	A
I_{SC}	Short-circuit current	A
I_t	light intensity entering the loss material	W/m^2
J	Current density	A/m^2
k	Imaginary part of refractive Index	-

k_{cond}	Thermal conductivity	W/(mK)
l	Finger length	m
m	Ideality factor	-
n	Real part of refractive Index	-
N	Complex representation of refractive index	-
oc	Open-circuit	-
P_{em}	Emitter power loss	W
P_m	Maximum power	W
q_{cond}	Conductive heat flux	W/m^2
q_{conv}	Convective heat flux	W/m^2
q_{rad}	Radiative heat flux	W/m^2
q_u	Useful heat energy	W/m^2
Q	Internal heat generation	W/m^2
r	Position vector	m
r_p	P-type reflection coefficient	-
r_s	S-type reflection coefficient	-
R_e	Emitter resistance	Ω
R_{sh}	Shunt resistance	Ω
R_P	P-type reflection power coefficient	-
R_{se}	Series resistance	Ω
R_S	S-type reflection power coefficient	-
sc	Short-circuit	-
t_p	P-type transmission coefficient	-
t_s	S-type transmission coefficient	-
T	Temperature	K
T_{amb}	Ambient temperature	K
T_c	Cell temperature	K
T_P	P-type transmission power coefficient	-
T_{ref}	Reference temperature	K
T_S	S-type transmission power coefficient	-
v	Wind velocity	m/s
V_m	Maximum power point voltage	V
V_{OC}	Open circuit voltage	V
V_T	Thermal voltage	V
y	Distance of element from cell-center	m

ABBREVIATIONS

AM	Air Mass ratio
AR	Anti-Reflecting
CPV	Concentrated Photovoltaic
CTM	Cell-To-Module
DNI	Direct Normal Irradiance
EVA	Ethylene Vinyl Acetate
FEA	Finite Element Analysis
FEM	Finite Element Method
FF	Fill Factor
GHI	Global Horizontal Irradiance
HPC	High Performance Computing
IEC	International Electrotechnical Commission
IR	Infrared
ISE	Institute for Solar Energy Systems
NOCT	Nominal Operating Cell Temperature
PDE	Partial Differential Equations
PV	Photovoltaic
STC	Standard Testing Conditions
UV	Ultraviolet

LIST OF FIGURES

LIST OF TABLES

1 INTRODUCTION

Like most real world systems, Photovoltaic (PV) modules are subjected to a multitude of physical phenomena. For a better understanding of the system, it is important to realize the process flow in an interlinked multiphysics problem. Most numerical studies conducted on PV modules found in literature, focus on one of the underlying physics phenomenon. With the help of new Finite Element Method (FEM) software packages and High Performance Computing (HPC) systems, it is possible to study coupled multiphysical problems accurately. In this work, multiphysics studies comprising ray-tracing, heat transfer and electric current tools are conducted on PV module using the FEM based software COMSOL Multiphysics®. Additionally, the ray-tracing tool is independently used to investigate the performance of new structures for PV-glass proposed in this work.

Solar cells used for electricity generation are fragile and so are embedded into protective structures collectively known as Photovoltaic (PV) modules. Though a PV module is important for the longevity and safety of the bare solar cells, it lowers the system efficiency (typically Cell-to-module (CTM) efficiency gap is above 10% relative (Haedrich, et. al., 2014) [1]). As shown by latest results (Trina Solar, 2015 [2]), a record module efficiency of 19.2% is achieved for P-type polycrystalline silicon cells, which have a cell efficiency of 21.25%. The CTM losses can be mainly categorized as [1]:

- Optical losses due to inactive module area and also due to the reflection and absorption of energy in the different layers of a PV module.
- Electrical ohmic losses in the different cell components.
- Thermal losses: a PV module due to its constituent components does not dissipate heat as efficiently as a bare solar cell. This leads to a higher cell temperature which lowers the operating voltage and hence the power (Skoplaki, et al., 2009) [3].

Reflection losses in fixed (non-tracking) PV installations increase for lower elevation angles (refer to figure 3.3). In a study, Sjerps-Koomen, et al., 1996 [4], found that for vertically mounted PV modules near the equator, yearly reflection losses due to lower elevation angles relative to Standard Test Conditions (STC) can be as high as 8%. In order to reduce reflection losses in PV modules, glass structuring has been proposed by various authors (Duell and Ebert, 2010 [5]; Nositschka, 2008 [6]; Krauter, 1993 [7]). Structuring a glass surface prevents the reflected light to be completely lost by directing it to the neighboring surfaces, where it again undergoes reflection and refraction. The phenomenon is illustrated in figure 1.1. Working along these lines, five pyramid-structured glass models are investigated using the ray-tracing tool in chapter 3. Their performance is compared to flat glass of a standard module.

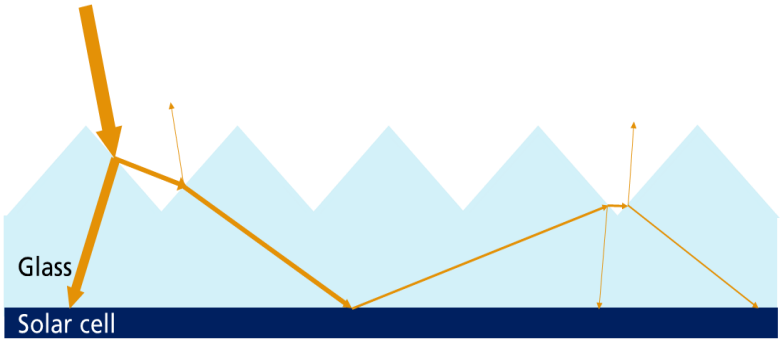

Figure 1.1: Light trapping in a structured glass (not to scale); ray undergoes multiple reflections due to the pyramid-like glass structures, thereby reducing the solar energy finally lost in reflection

In chapter 4 thermal analysis of a one-cell PV module is conducted using a multiphysics study. The solar energy absorbed by PV cells is converted into electric and thermal energy. Due to the absorbed thermal energy, operating temperature of the solar cells increases. Since, the efficiency of the PV solar cells is inversely proportional to the cell temperature (Green, 1982) [8], it is important to determine the temperature of the solar cells in the PV module. Zhou, et al., 2015 [9]; Usama Siddiqui, et al., 2012 [10]; Lee, Y., et. al. 2012 [11] have conducted studies to analyze the temperature distribution of PV modules in the past.

All of these studies determine the heat absorbed in the different module components based on constant optical coefficients (reflectance, transmittance and absorbance). These coefficients however vary significantly with the incidence angle of the irradiation. For instance the reflection coefficient of glass can vary in a range of 0.04 to 1. In the model presented, absorption of solar energy in the materials is measured with the help of ray optics tool, which allows analysis for any incidence angle. The attenuation in energy of solar rays as they are absorbed in the different materials is calculated in the optical study. Thus using a multiphysics simulation, heat absorbed in the module can be accurately calculated by optical simulation and used as input for thermal study of PV modules.

Chapter 5 focuses on the electric (ohmic) losses occurring in the solar cell due to the inherent resistances of the cell components. Charge carriers in a cell that are excited by solar energy have to be evacuated before they recombine or release their energy. In a PV module, the fingers, busbars and ribbons form a grid network that enables a current flow in the external circuit. In certain PV systems such as bifacial PV modules, concentrated PV and modules with structured-glass, the cell illumination is inhomogeneous (Johnston, 1998) [12]. Due to this inhomogeneity in illumination, the magnitude of current generated is also not uniform over cell surface. There is a higher current density generated in the brightly lit parts of such a cell. Ohmic losses are proportional by a power of two to current density. Thus in order to keep the electrical losses down, a non-uniformly distributed metal grid for inhomogeneous cell irradiance is

modeled and studied using FEM based electrical simulation. The electrical simulation is coupled with the optical study to compute the performance of the proposed grid.

Chapter 6 describes outdoor experiments carried out on a one-cell PV module and multiphysics study of the PV module to validate the accuracy of FEM simulations. The module is tested with different illumination patterns, which are generated with the help of opaque masks. The experiment conducted on the PV-module involves a coupling of two physical processes, namely:

- Absorption of solar energy by the module,
- Heat dissipation from the module.

Multiphysics study comprising ray-tracing and heat transfer tools are used in the simulations to represent the above mentioned processes.

Chapter 7 summarizes and identifies the role of multiphysics simulation to study PV modules. Recommendations for further research are also discussed.

In the next chapter the basics of PV modules and Finite Element Method (FEM) are reviewed. Also, the theory and governing equations of ray optics, heat transfer and electric losses, which are studied using FEM simulations in this thesis, are briefly discussed.

2 THEORETICAL BACKGROUND

2.1 Photovoltaic modules

Photovoltaic (PV) effect is the basic principle of the working of a solar cell. Solar energy absorbed by a solar cell is converted into electrical energy. A standard Silicon PV module consists of many solar cells interconnected in serial and in parallel. A series interconnection leads to a higher voltage across the terminals whereas a parallel interconnection increases the current rating of the module. To protect the solar cell from ingress of water or other contaminants and to provide mechanical strength to the module, solar cells are covered on both the sides.

2.1.1 Standard modules:

A Photovoltaic module consists of the solar cell along with other components as shown in figure 2.1 and discussed in the following sub-sections. The outer edges are sealed for weatherproofing and stability, for which often an aluminum frame is used. A junction box for electrical connections and for holding bypass diodes is placed at the back of the module.

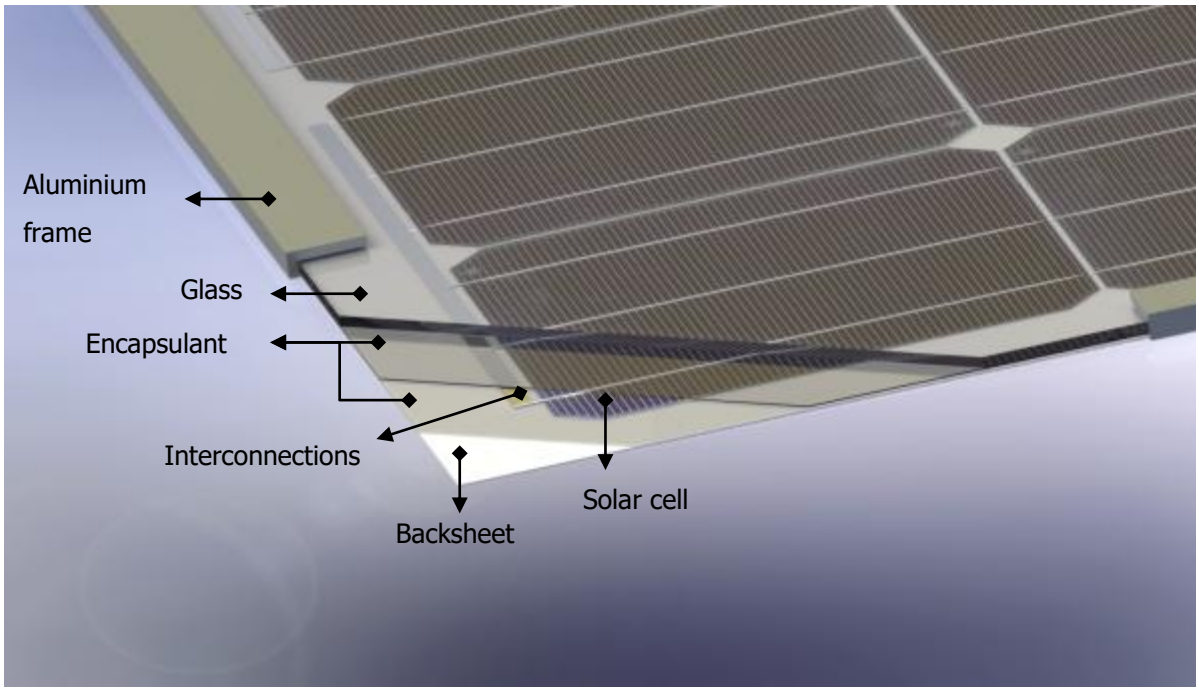

Figure 2.1: Cut-section of a standard PV module showing the different components (Fraunhofer ISE)

2.1.1.1 Solar cell

Basically a large area p-n junction diode, solar cells can be produced from various materials, but the most commonly used material is Silicon. A Si-based solar cell is a thin wafer consisting of two oppositely-doped layers which include a shallow n-type region and a p-type bulk region. Due to movement of the majority charge carriers across the boundary of the two layers, an electric field is developed between the n-region and p-region. Photons absorbed by the cell from solar energy excite electrons from valence band to the conduction band. The excited electron is pulled back into the n-region by the electric field. Similarly generated holes move to the p-region. Externally connecting the solar cell establishes a current flow.

The energy required to excite charge carriers depend on the band gap (1.1 eV for Silicon) of the solar cell. Photon energies less than the band gap are not sufficient to excite an electron from the valence band to the conduction band. Also, not all the excited electrons contribute to electricity generation as some of them recombine with the holes (Quaschning, 2005) [13]. An electrical representation of a solar cell can be described by a double-diode model shown in figure 2.2 and defined by equation 2.1. (Wolf, et al., 1963) [14].

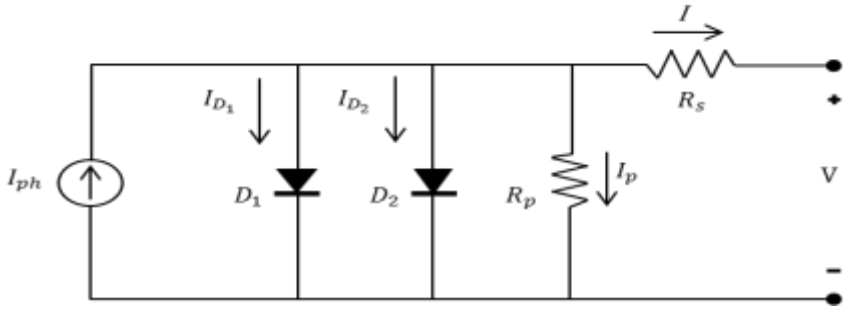

Figure 2.2: Equivalent circuit of a solar cell as a double-diode model [14]

$$I(V) = I_{ph} - I_{s1}.\left(exp\left(\frac{V + IR_{se}}{m_1.V_T}\right) - 1\right) - I_{s2}.\left(exp\left(\frac{V + IR_{se}}{m_2.V_T}\right) - 1\right) - \frac{V + IR_{se}}{R_{sh}} \qquad (2.1)$$

where I_{ph} is the photocurrent, which depends on the irradiance

I_{s1}, m_1: Diode 1 saturation current and ideality factor respectively

I_{s2}, m_2: Diode 2 saturation current and ideality factor respectively

V_T is the Thermal voltage; at 25 °C, V_T = 25.7 mV

R_{se}, R_{sh} are the series and shunt resistances respectively

In this thesis, the electrical modeling of the solar cell is limited to ohmic losses. A subject of further study and research can be to incorporate the double-diode model to develop a tool to simulate the electrical behavior of the solar cell.

2.1.1.2 Glass

For the front surface, toughened solar grade glass is typically used. The front glass must have a high transmittance for the absorption spectrum of the solar cell material and the sun spectrum. In order to reduce reflections from the glass surface, anti-reflective coatings are applied on the glass. Also to reduce absorption of solar energy in the glass, thickness can be reduced provided that the glass is able to withstand the harsh environmental conditions and other mechanical stresses that the module may be exposed to.

Low-iron glass is most commonly used due to its low cost, stability under prolonged Ultraviolet (UV) exposure, higher transparency, self-cleaning properties, and imperviousness to water and other contaminants that may cause degradation of the solar cell. Currently, typical thickness of glass used in PV modules is 3.2 mm.

2.1.1.3 Encapsulant

Solar cells are sandwiched between encapsulant layers that provide adhesion between the top glass, solar cells, and the rear surface. A flexible layer, encapsulant reduces mechanical stresses and helps in absorbing shocks and vibrations, thereby protecting the solar cell. The encapsulant layer must have lower reflectivity and absorptivity to keep the optical losses down. The cross-linkable polymer Ethylene Vinyl Acetate (EVA) is the most commonly used encapsulant material. With the help of a laminator, the solar cells are laminated between EVA films under vacuum and at a temperature of around 150 ^{o}C (Wirth, 2012) [15].

2.1.1.4 Backsheet

While avoiding ingress of moisture and providing electrical insulation, the backsheet must be able to diminish the ultraviolet radiations reaching the EVA polymer which is less stable to UV exposures. As a rear cover, a thin polymer sheet, usually Tedlar is used in photovoltaic modules. In case of bifacial PV modules, both the front and the back covers are optically transparent.

2.1.1.5 Interconnections

To establish a current flow in the cell, an external circuit is formed by the metal interconnections. Tin alloy

coated copped ribbons are most commonly used for interconnecting the solar cells. These ribbons are soldered over the silver-based busbar network of the cells. The current generated in the solar cell is carried to the junction box by the interconnection ribbons. Since ribbons cause shading and ohmic losses, due consideration is given to its width and cross-section.

2.1.2 Relation between cell temperature and electrical efficiency

Temperature of a PV module depends on the incoming solar irradiation, electrical efficiency, optical and thermal properties of the components and heat exchange with the surroundings (Villalva, et al., 2009) [16]. Temperature affects the maximum power generated by the solar cell, which is given by equation 2.2:

$$P_m = V_m I_m = (FF) V_{OC} I_{SC} \tag{2.2}$$

where the subscript *m* implies maximum power point of the I-V curve,

P, V, and I refer to power, voltage and current respectively,

FF gives the fill factor of the module and

subscripts *oc* and *sc* refer to the open-circuit and short-circuit conditions.

Both the open-circuit voltage and the fill factor decreases substantially with temperature; the short-circuit current increases but only slightly with temperature (Zondag, 2008) [17]. The net effect is a decrease of power and efficiency and can be given by the linear relation 2.3 (Evans, 1981) [18]:

$$\eta_c = \eta_{ref}[1 - \beta(T_c - T_{ref})] \tag{2.3}$$

where η_{ref} is the module efficiency at reference temperature, T_{ref}

β is the temperature coefficient, for silicon cells β is 0.0045 K^{-1} [17], and

T_c is the cell temperature.

2.2 Finite Element Method (FEM)

Most real world space- and time- dependent problems can be expressed by partial differential equations (PDEs). In most cases, the problems are so complex that it is almost impossible or impractical to solve the

PDEs using analytical methods. In such cases, numerical methods can provide approximate solutions to the physical problems. The problem is suitably discretized which can then be solved by the numerical methods. The accuracy of the solution depends on the degree of discretization. Finite Element Method (FEM) or Finite Element Analysis (FEA) is one such numerical method.

To perform a finite element analysis, a mathematical model of the physical problem is realized. The steps involved for the analysis can be demonstrated by figure 2.3.

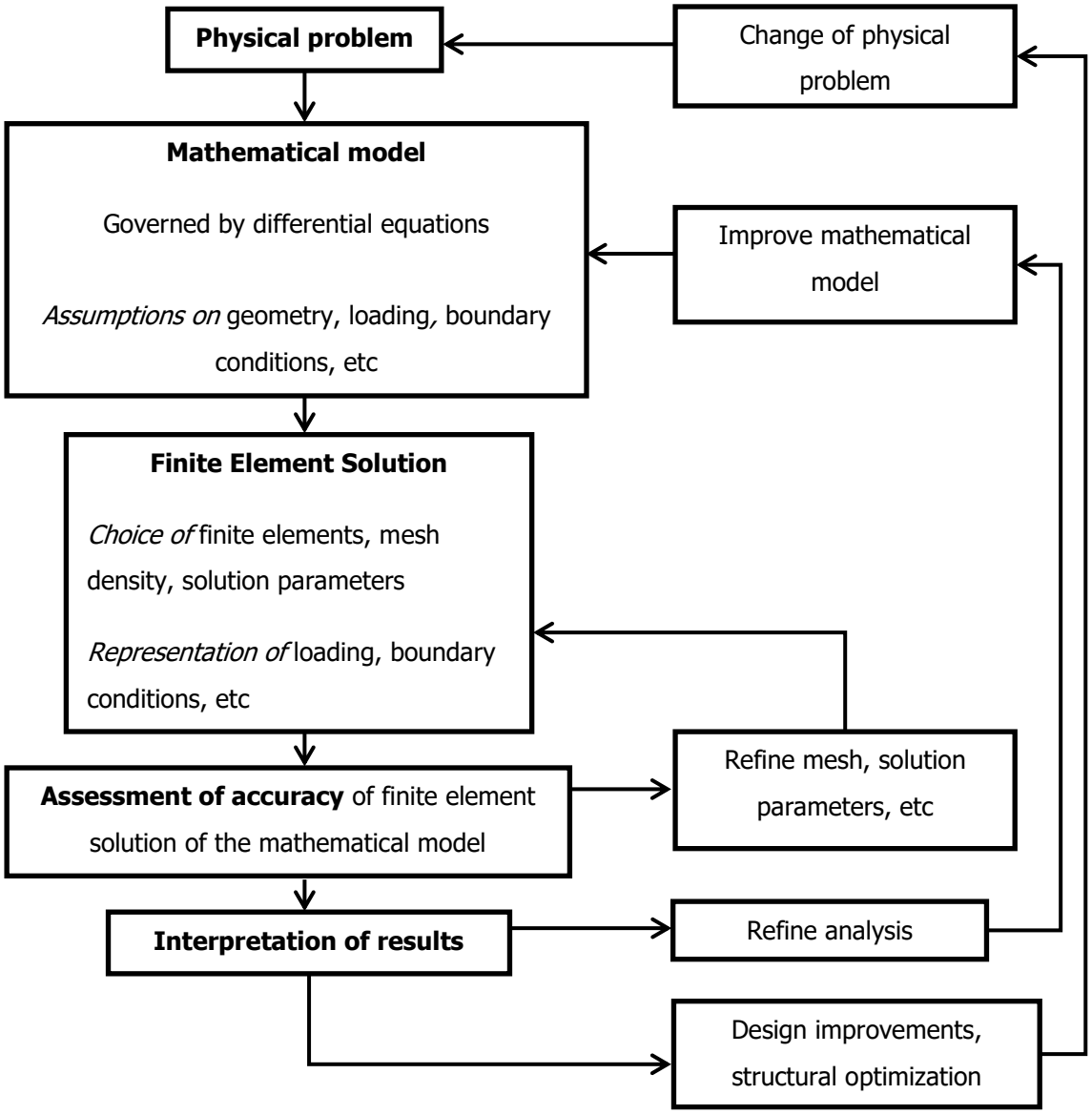

Figure 2.3: Different steps involved to perform a Finite Element Analysis (Bathe, 1996) [19]

The purpose of finite element analysis software is to reduce the number of prototypes and experiments that have to be run when designing, optimizing, or controlling a device or a process. Once an FEM model is established and has been found useful in predicting the functioning of a system, it may generate the understanding and intuition to significantly improve the design and operation of the system. Due to these reasons, FEM is an integral tool for the research and development departments in institutions and companies. The simulations presented in this thesis are carried out in the software- COMSOL Multiphysics®.

As in any real process, where several physical phenomena couple together, COMSOL enables the integration of multi-physics. The software provides inbuilt definition of the governing equations for the various physical phenomena that can be simulated in it. Further, there is a large database of material properties. The process involved in setting up a simulation to evaluate the results can be summarized as below:

- **Model generation:** As a first step, the model geometry for the system under study is prepared. Depending on the symmetry of the system, a 3-D structure can be reduced to a 3-D axisymmetric or a 2-D model, which may drastically reduce the computational burden. It is important to mention here that for analysis, all the surfaces have to actually form a real volume.

- **Assigning materials:** Different parts of the model are attributed with the respective materials that constitute the physical entity being modeled. The governing equations and the constitutive relations of the mathematical model depend on the physical properties of the material.

- **Boundary conditions:** Defining the initial and boundary conditions constitute a vital step in the modeling process. The boundary conditions represent the loading on the system and other constraints that are imposed on the real system. The boundary conditions along with the governing equations are used to obtain a numerical solution. A particular model can be simulated for infinite number of initial and boundary value conditions. However, to make the model uniquely representative of the system, appropriate set of conditions are to be imposed on the model.

- **Meshing:** FEM works by discretizing the entire geometry into smaller elements. The numerical computations are carried out in these elements, which are later conjoined to form a global solution. Depending on the area of interest, mesh densities can be varied over the different parts of the geometry.

Generally, mesh density determines the accuracy of the solution. Assuming that there are no singularities, a denser mesh would generate a closer approximation of the exact solution. However, a finer mesh will require larger computer memory and longer run times. Also, for an accurate result, it is very important to keep the aspect ratios of the elements low. The maximum aspect ratio used in the model varies from case to case. For the models studied here, the aspect ratios were kept within 15:1.

Figure 2.4 shows the meshing of a standard PV module. Since analysis of the solar cell is most important, the model is finely meshed at the cell than at the other components.

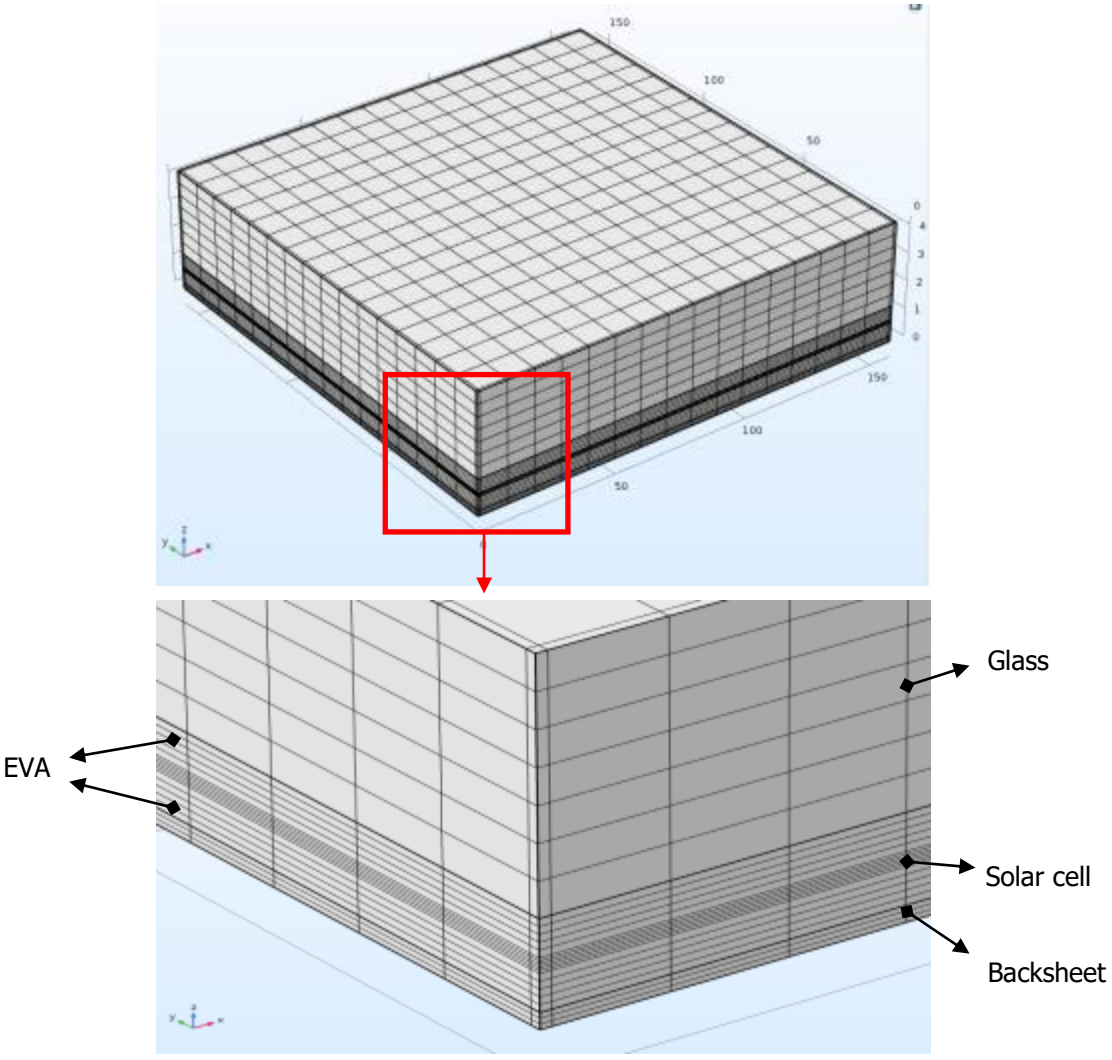

Figure 2.4: Mesh of a model for FEM study; level of discretization in a specific part depends on the importance of the part on the particular study

- **Study:** Depending on the problem, the meshed geometrical model is now studied. Using the software COMSOL Multiphysics, various types of studies can be performed, which include:
    - Stationary and transient studies
    - Linear and non-linear studies
    - Eigen frequency, modal, and frequency response studies

In this step, the solver is configured for the simulation. The solvers break down each problem — linear or nonlinear — into one or several linear systems of equations by approximating the given problem with a linearized problem. The coefficient matrix of the discretized linearized problem is called the Jacobian matrix (or stiffness matrix).

- **Post processing:** The intended output is extracted from the multitude of the results generated by the simulation. An important task in post processing is to perform a mesh convergence study. This can be done by varying the mesh sizes and comparing the solutions so obtained. The error between the approximated result and the exact solution must decrease as the mesh becomes denser. This is shown in the figure 2.5. For simulations in this work, models were studied with increasingly denser mesh, until the results produced no significant improvement.

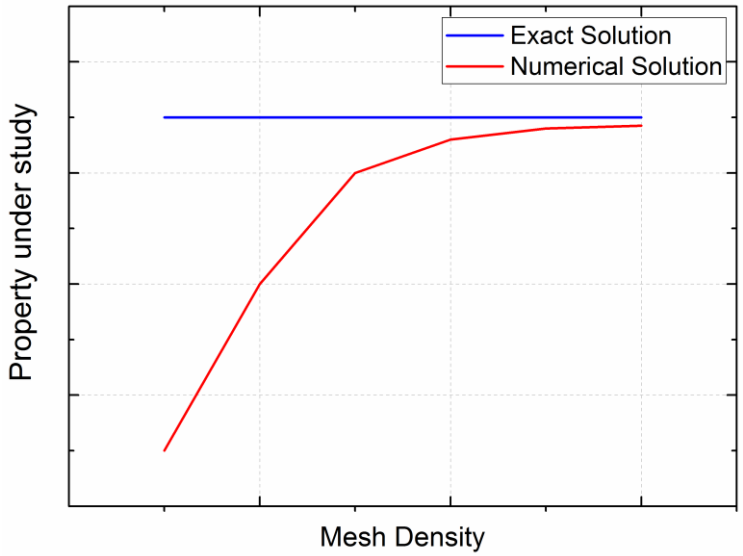

Figure 2.5: Mesh convergence study for a numerical solution (Zienkiewicz, 1977) [20]; increasing mesh density reduces difference between numerical solution and exact solution

2.3 Ray optics

This section describes the basics of ray optics which form the underlying principle of the optical simulations. Ray optics specifies light as rays that travel in different optical media in accordance with a set of geometrical rules (Saleh, et al., 1991) [21]. Ray optics is therefore also called geometrical optics. The postulates governing ray optics can be described as below [21]:

- Light travels in the form of rays.

- An optical medium is characterized by refractive index, n. Light travels in a medium with a speed $c = c_0/n$, where c_0 is the speed of light in free space. The time taken by light to travel a distance of d is given by d/c or nd/c_0. The product nd is called optical path length

- In an inhomogeneous medium, the refractive index $n(r)$ is dependent on the position $r(x, y, z)$ in the optical medium. The optical path length along a given path *A* to *B* in an inhomogeneous medium is given by

  Optical path length $= \int_A^B nds$

  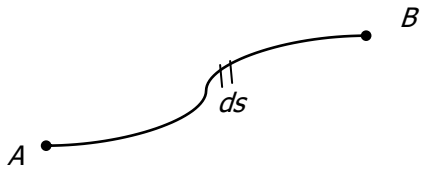

  where, ds is the differential length element along the given path.

- Fermat's principle: It states that a light ray travels between two points along a path that will require the least time among other nearby paths. Fermat's principle can be used to derive the laws of reflection and refraction.

When a light ray falls on an interface separating two different optical media, it can undergo any or a combination of the following:

- Partial or total reflection at the interface
- Refraction, whereby the light ray enters the second medium

2.3.1 Reflection of light

When a ray of light is reflected back from a plane surface, the angle of reflection (θ_r) that the reflected ray subtends to the normal of the surface is equal to the angle of incidence (θ_i) given by equation 2.4 (Born, et al., 2003) [22].

$$\theta_r = \theta_i \tag{2.4}$$

The incident ray and the reflected ray lie in the same plan. These are known as the laws of reflection.

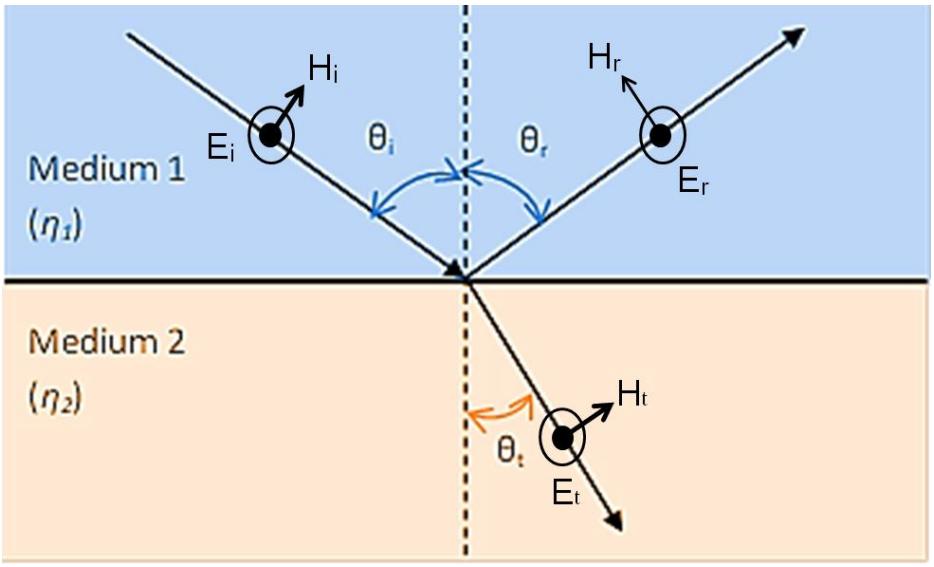

Figure 2.6: Reflection and refraction of light on a plane surface when an incident ray strikes an interface between two media of different refractive indices

2.3.2 Refraction of light

A light ray incident on an interface separating two different optical media may transmit to the second medium via refraction. The refracted ray lies in the plane of the incident ray. However, the speed of light in the media differs and is dependent on the refractive index, n. The path of the refracted ray in the second medium is dependent on the incident angle and on the refractive indices of the interacting media. The relation between the incident and refracted angles and the refractive indices of the media is given by equation 2.5. (Snell's Law).

$$n_1 \sin\theta_i = n_2 \sin\theta_t \tag{2.5}$$

where n_1 and $n_2$are the refractive indices of medium 1 and 2 respectively, and

Angles θ_i and θ_t are the incident and transmitted (refracted) angles respectively.

2.3.3 Fresnel equations

The fraction of the light ray that is transmitted or refracted and that reflected when a light ray falls on an interface separating two different optical media are given by Fresnel equations. Fresnel equations can be derived with the help of Snell's law and the boundary conditions of the electric and magnetic fields in the media. Since the electromagnetic wave is transverse, the behavior depends on the polarizations of the incident ray. The polarization components can be decomposed into S-type (electric field of the incident ray perpendicular to the plane of incidence - plane containing the incident, reflected, and refracted rays) and P-type (electric field of the incident ray parallel to the plane of incidence).

Considering a light ray incident on a media interface undergoes both reflection and refraction as shown in figure 2.6, as per the laws of reflection, the reflected and refracted angles are given by the equation 2.4 and 2.5. The reflection and transmission coefficients for the polarizations are given by equation 2.6-2.13. (Born, et al., 2003 [22], Saleh, et al., 1991 [21], Krauter, 1993 [7])

For a P-Polarized light ray:

Reflectance coefficient,

$$r_p = \frac{n_1 \cos\theta_t - n_2 \cos\theta_i}{n_1 \cos\theta_t + n_2 \cos\theta_i} \tag{2.6}$$

Transmission coefficient,

$$t_p = 1 - r_p = \frac{2n_1 \cos\theta_t}{n_1 \cos\theta_t + n_2 \cos\theta_i} \tag{2.7}$$

Power (or Intensity) coefficients,

$$R_P = |r_p|^2 \tag{2.8a}$$

$$T_P = |t_p|^2 \tag{2.8b}$$

Similarly for an S-Polarized light ray:

Reflectance coefficient,

$$r_s = \frac{n_1 \cos\theta_i - n_2 \cos\theta_t}{n_1 \cos\theta_i + n_2 \cos\theta_t} \tag{2.9}$$

Transmission coefficient,

$$t_s = 1 - r_s = \frac{2n_1 \cos\theta_i}{n_1 \cos\theta_i + n_2 \cos\theta_t} \tag{2.10}$$

Power (or Intensity) coefficients,

$$R_S = |r_s|^2 \tag{2.11a}$$

$$T_S = |t_s|^2 \tag{2.11b}$$

For unpolarized light, the power coefficients are given as:

$$R = \frac{1}{2}(R_S + R_P) \tag{2.12}$$

$$T = 1 - R \tag{2.13}$$

Using the equations (2.4-2.13), intensity of the reflected and transmitted rays in terms of fraction of the incident intensity is calculated and plotted in figure 2.7.

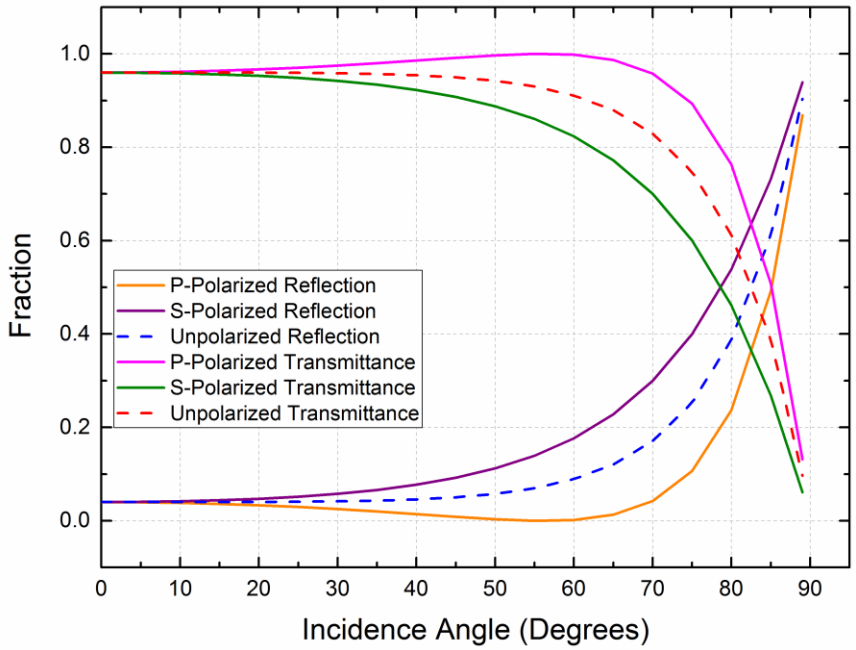

Figure 2.7: Reflection and transmission power coefficients for media with refractive indices n_1=1 and n_2=1.5. Reflection increases considerably for incidence angles higher than 55°.

From the figure 2.7, one can clearly see that for incidence angles higher than 55° reflection coefficients

increases considerably. For unpolarized light, values of reflection and transmittance coefficients are given by the average of those of P-polarized and S-polarized light rays.

2.3.4 Absorption of light in a medium

The relations obtained so far are relevant for non-absorbing media. The intensity of a light ray passing through a medium may attenuate in different degrees depending on the medium. For absorbing media, this lost energy of the light ray is imparted to the medium in the form of thermal or other forms of molecular energy. Absorption of light in the medium can be taken into account by incorporating complex part in the refractive index as shown by equation 2.14 (Born, et al., 2003) [22].

$$N = n + ik \tag{2.14}$$

where the effective refractive index of an absorbing medium, N consists of

real part n, which gives the ratio of the speed of light in free space to the phase velocity of light in the medium and is defined as $n = c_0/c$, and

imaginary part k due to absorption is called the extinction coefficient.

For a non-absorbing material, the extinction coefficient, k = 0. Both the real and the imaginary part of the refractive index are dependent on the wavelength of the light ray.

A light beam of intensity I_t transmitted in an absorbing medium will have an attenuated intensity after passing through the medium. The attenuation in intensity due to absorption follows an exponential curve given by equation 2.15 (Duffie, et al., 2006) [23].

$$I = I_t \, exp\,(-\frac{\alpha d}{cos\,\theta_t}) \tag{2.15}$$

where, I_t is the light intensity entering the loss material,

I is the light intensity at the end of loss material,

α is the absorption coefficient of the material,

d is the thickness of the material, and

θ_t is the angle of refraction

Absorption coefficient of a material, α is a function of the extinction coefficient, k and the wavelengthλ:

$$\alpha = \frac{4\pi k}{\lambda} \tag{2.16}$$

The light intensity transmitted to a medium when a beam undergoes both reflection and refraction at the interface of two media is given by equation 2.17. [23]

$$I_t = I_0\,(1 - R) \tag{2.17}$$

where I_0 is the intensity of light incident on the interface of the media, and

R is the reflection coefficient given by equation 2.12.

Therefore, accounting for both reflection at the interface and absorption in the medium, intensity of light ray after travelling a distance d in the medium is given by equation 2.18. [23]

$$I = I_0\,(1 - R)\,exp\,(-\frac{\alpha d}{cos\,\theta_t}) \tag{2.18}$$

2.4 Heat transfer

Solar energy absorbed by the PV cells which is not converted into electrical energy is released in the form of thermal energy. The cell, thus acts as a heat source. The operating temperature of a PV module is reached when equilibrium is established between the heat generated by the solar cell and heat lost to the surrounding via conduction, convection and radiation. The performance of a solar cell is largely dependent on temperature among other factors (Green, 1982) [8] and the dependence of efficiency on temperature is given by eq. 2.3. In this section, basic theory of the three heat transfer modes is briefly discussed.

2.4.1 Heat conduction

Solid bodies in contact and having a temperature gradient between them, experience a flow of heat from a higher potential to a lower potential until equilibrium is reached. The different amount of heat absorbed by the module components and thermal conductivity of the components give rise to heat transfer in the form of conduction.

In a continuous medium, Fourier's law of heat conduction states that the conductive heat flux q_{cond} is proportional to the temperature gradient and is given by equation 2.19

$$q_{cond} = -k_{cond}\nabla T \tag{2.19}$$

where q_{cond} is the conductive heat flux,

k_{cond} is the thermal conductivity, and ∇T is the temperature gradient

Energy transferred by conduction depends on the thermal resistance of the materials in contact.

The coefficient of proportionality k_{cond}, takes a positive value meaning heat flows from regions of high temperature to low temperature. More generally the thermal conductivity can take the form of a symmetric positive-defined second-order tensor in anisotropic media such as composite materials:

$$k_{cond} = \begin{bmatrix} k_{xx} & k_{xy} & k_{xz} \\ k_{yx} & k_{yy} & k_{yz} \\ k_{zx} & k_{zy} & k_{zz} \end{bmatrix} \tag{2.20}$$

2.4.2 Heat convection

Movement of air over the surfaces of the PV module that are exposed to the environment gives rise to convective heat transfer. The wind speed at the location of the module and the ambient temperature affects this form of energy transfer. The mathematical relation of convection can be represented by equation 2.21 (Newton's law of cooling)

$$q_{conv} = h(T - T_{amb}) \tag{2.21}$$

where q_{conv} is the heat flow due to convection, h is the convective heat transfer coefficient,

T is the temperature of the exposed surface, and T_{amb} is the ambient temperature.

Convective heat transfer coefficient, h, is dependent on the wind velocity and the relation is given by equation 2.22 (Notton, et al., 2005) [24].

$$h = 5.82 + 4.07\, v \tag{2.22}$$

where the wind speed is given by v (in meters per second).

2.4.3 Radiation

Thermal radiation is the transfer of energy in the form of electromagnetic waves. Unlike other forms of heat transfer, radiation does not require a medium. All objects above absolute temperature emit energy in the form of radiation. It is strongly related to the temperature of the emitting object. Thermal radiation is governed by Stefan-Boltzmann Law. Heat transfer between the PV module and the environment due to radiation can be defined by equation 2.23 (Stefan-Boltzmann Law).

$$q_{rad} = \varepsilon\sigma(T^4 - T_{amb}^4) \tag{2.23}$$

where q_{rad} is the heat transfer due to radiation,

ε is the emissivity of the surface. For a perfect emitter or a blackbody, $\varepsilon = 1$,

σ is the Stefan-Boltzmann constant,

T is the temperature of the PV module, and

T_{amb} is the ambient temperature

The relation for radiative heat transfer holds true if the temperature around the PV modules can be considered equal to the ambient temperature.

2.4.4 Heat balance equation

Combining all the elements, governing equation for heat transfer in PV modules can be expressed by equation 2.24 (Sundén, 2012) [25]

$$q_u = q_{cond} - (q_{rad} + q_{conv}) \tag{2.24}$$

where q_u is the useful energy absorbed by the solar cell,

$q_{cond}, q_{rad}, q_{conv}$ are the conductive, radiative and convective heat flux respectively.

2.5 Electric (ohmic) losses

A solar cell cross-section with series resistance contributions of different cell elements is shown in figure 2.8. Current generated in the solar cell pass from the rear metalized surface, vertically through the bulk to the emitter where it flows laterally into the finger, from the finger to the busbar and finally into the interconnecting ribbon from the busbar (Franklin, et al., 2002) [25].

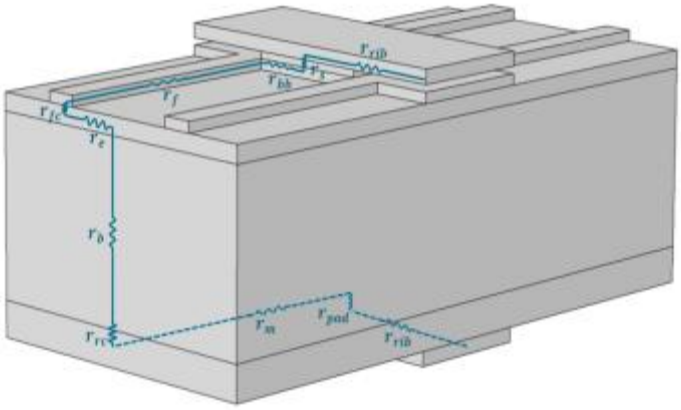

r_{rib}: Ribbon resistance
$r_{s:}$ Solder resistance
r_{bb}: Busbar resistance
r_f: Finger resistance
r_{fc}: Contact resistance of front grid to emitter
r_e: Emitter resistance
r_b: Base resistance
r_{rc}: Contact resistance of rear grid to base
r_{pad}: Resistance of silver pad
r_m: Resistance of metal layer

Figure 2.8: Cross-section of a solar cell (not to scale) showing different series resistance contributors (Mette, A. 2007) [26]

The total series resistance of the cell is given by the sum of all the individual component resistances. Power losses in contact resistances and base resistance are typically much smaller than those in the emitter and metallization (Haas, et al., 2014) [27] and thus have been neglected for the simulations in this work. A significant power loss and reduction in open-circuit voltage due to the thin sheet resistance emitter layer is reported by many studies (Smirnov, et al., 1980 [28]; Mitchell, 1977 [29]; Franklin, et al., 2002 [25]). A non-uniform illumination augments the loss [27]. Using FEM electrical study, ohmic loss due to any individual series resistance component or for the entire cell can be calculated, however in this work loss only due to emitter resistance is computed.

Emitter power loss

Electric loss (dP_{em}) in an infinitesimally small section dx of the emitter surface, shown in figure 2.9 is given by equation 2.25

$$dP_{em} = I^2 dR_e \tag{2.25}$$

where the differential resistance, dR_e is given by equation 2.26

$$dR_e = \rho_e \frac{dx}{l} \tag{2.26}$$

where ρ_e is the emitter sheet resistivity in Ω/square, and

l is the finger length given by the distance between the finger edge and busbar as shown in the figure 2.9.

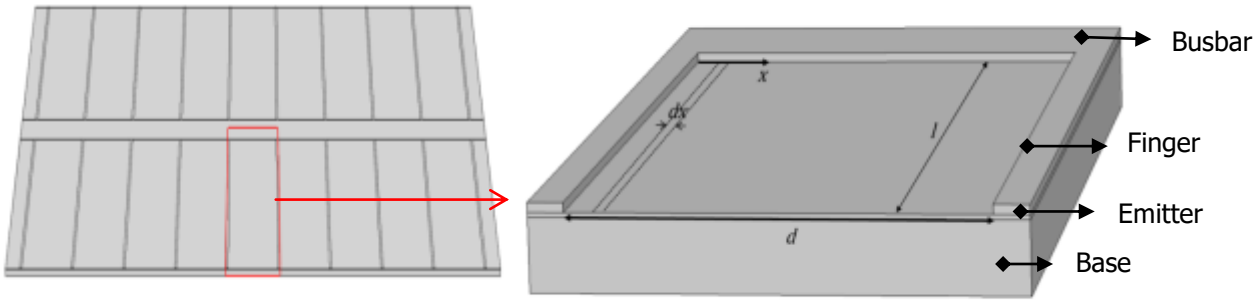

Figure 2.9: A small cross-section of a solar cell. Power loss due to lateral current flow in the emitter layer of the cross-section is evaluated based on this figure.

Under uniform illumination, the lateral current flow, $I(x)$ in the emitter is a spatial function given by equation 2.27; its magnitude linearly increasing from zero at the center of the distance to its adjacent fingers to a maximum value at the finger boundary.

$$I(x) = J.l.x \tag{2.27}$$

where J is the current density due to the illumination.

The total power loss, P_{em} in the emitter region due to lateral current flow in the model shown in figure 2.9 can be obtained by integrating equation 2.25 over the entire surface

$$P_{em} = \int_{-d/2}^{d/2} I^2 \, dR_e = 2 \int_{0}^{d/2} J^2 \, l \, x^2 \rho_e dx = \frac{1}{12} J^2 l \, \rho_e {d_f}^3 \qquad (2.28)$$

where d_f is the distance between adjacent fingers.

From eq. 2.28, we can see that the emitter power loss depends proportionally on the finger length, emitter sheet resistivity, and depends strongly on current density and distance between the fingers.

For a homogeneous illumination, emitter loss can be easily calculated using the relation derived above. However, for an inhomogeneous illumination, where the current density can no longer be represented by the relation 2.27, it is difficult to calculate the power loss by analytical methods. With the help of FEM simulations, electrical loss in an inhomogeneous irradiated cell can be computed as the surface is discretized into fine elements. The performance of metal grid with non-uniform spacing between adjacent fingers is analyzed. The finger spacing at a cell position depends on the cell illumination at that position. Regions with higher irradiance are modeled to have closely spaced fingers. The effect of a modified grid is studied and the results are compared to a cell with a conventional metal grid.

3 OPTICAL MODEL

For a large fraction of PV modules on the market, glass forms the front cover and determines the amount of solar energy that reaches the cell. The glass used in a PV module must be such that its optical transmittance is high for the absorption spectrum of the solar cell material and the sun spectrum. Silicon solar cells have bandgap energy of 1.12 eV, which corresponds to a wavelength of 1.1 μm (Green, et. al., 1995) [30]. To excite an electron from the valence band to the conduction band, photon energies must be higher than the bandgap energy. Thus, light rays of wavelength higher than 1.1 μm are not converted into electricity by the silicon solar cell as the corresponding energy of the ray is lower than the bandgap energy.

The most commonly used representation of the solar irradiance is given by AM1.5 reference. The AM1.5 Spectrum is defined in the International Electrotechnical Commission (IEC) Norm for Standard Testing Conditions (STC) and is commonly used for comparability. Global (direct and diffused) AM1.5 irradiance spectrum and the absorption spectrum of a silicon solar cell are shown in the figure 3.1.

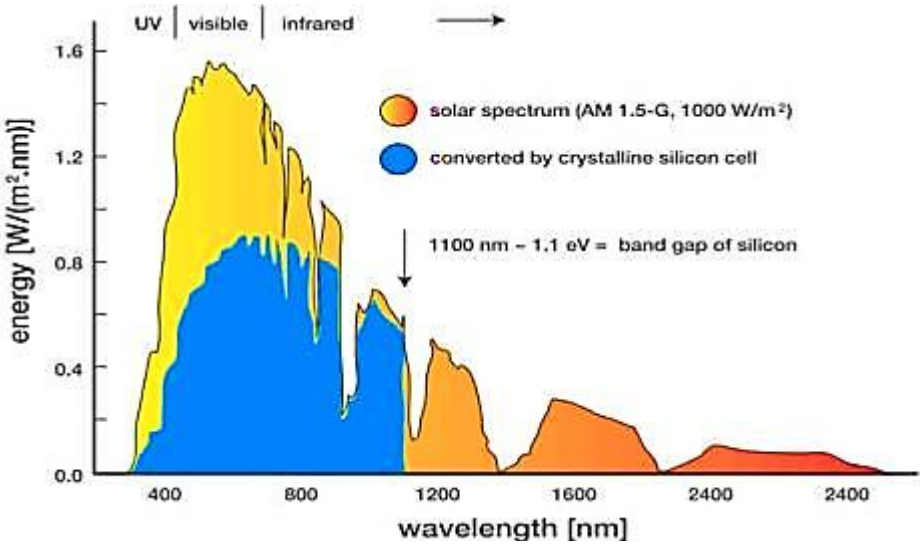

Figure 3.1: Solar spectrum (AM 1.5) and silicon absorption spectrum [31]

The material optical properties, refractive index and absorption coefficient are dependent on the wavelength. In this section, optical losses due to reflection at the air-glass interface and absorption in the glass medium are calculated using ray-tracing tool of FEM software COMSOL Multiphysics®.

To test the accuracy of the ray-tracing tool, first a simple model whose optical losses can be calculated analytically is simulated. The model simulated is that of a flat glass normally used in a standard solar PV

module. Low-iron soda lime glass has been used for the simulations. Since low-iron soda lime glass has almost uniform transmittance (figure 3.2) (Rubin, 1985) [32] over the spectral range of a silicon solar cells (350 nm to 1.1 μm) the optical study is conducted for one particular wavelength of 750 nm to minimize the computational time and resources.

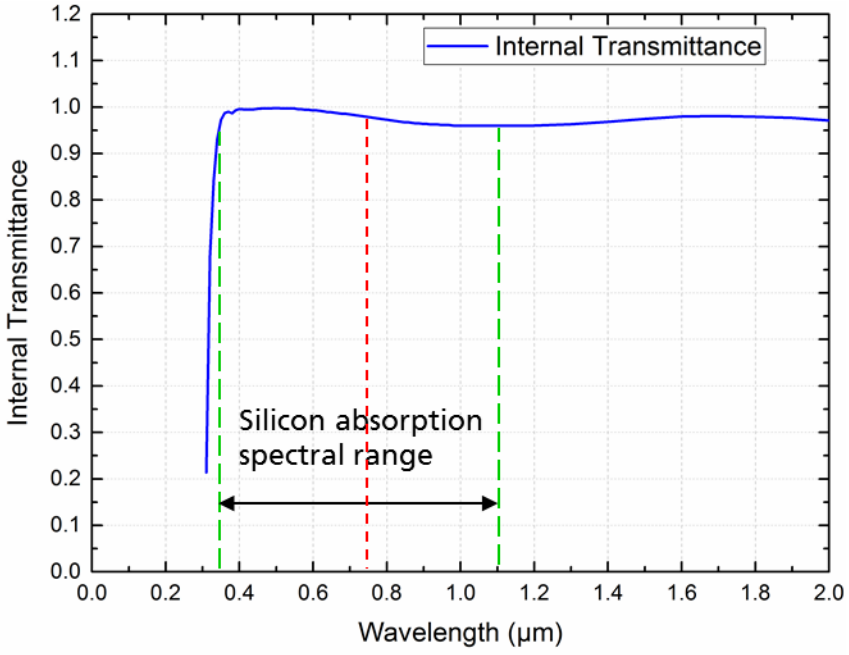

Figure 3.2: Transmittance of a 3.2 mm thick low-iron soda lime glass against wavelength (Rubin, 1985) [32]

The dimensions of the model and properties of the glass at a wavelength of 750 nm are mentioned in table 3.1.

Type of Glass	**Low-iron soda lime glass**
Thickness of the glass structure	3.2 mm
Refractive index, η	1.518 (Rubin, 1985) [32]
Extinction coefficient, k	4.067e-7 [32]
Absorption coefficient, α	0.068 cm^{-1}

Table 3.1: Properties of glass used for the optical simulation for a wavelength of 750 nm

3.1 Assumptions of the optical simulation:

The different assumptions considered for the optical simulations of a simple flat glass are mentioned as follows:

Parameters	Values
Solar Irradiance	1000 W/m^2
Wavelength of rays	750 nm
Elevation angles	90^o-15^o

Table 3.2: Assumptions considered for optical simulation of a flat low-iron soda lime glass

- Air and the glass medium are homogeneous and have their corresponding refractive index uniform over the silicon spectral range.
- The incident radiations are assumed to be unpolarized in nature.
- The glass surface is considered to be free of dust and dirt.
- Since rays are released from a surface area of the same dimensions as the glass surface, refraction of rays near the glass edge might not hit the base of the glass surface. Transmittance is thus calculated over a central area (as can be seen in figure 3.5) to avoid edge-effects that arise due to this fact.

3.2 Boundary conditions

Intensity of the transmitted ray through glass is strongly dependent on the incident angle. A ray of light can be completely characterized by two angles- elevation angle and azimuth angle. Elevation angle of a ray falling on a surface is given by the angle that the ray makes with the module surface. In this work, azimuth angle is considered to be the angle between the exact south and the plane containing the ray. Depiction of the elevation and azimuth angles is shown in figure 3.3.

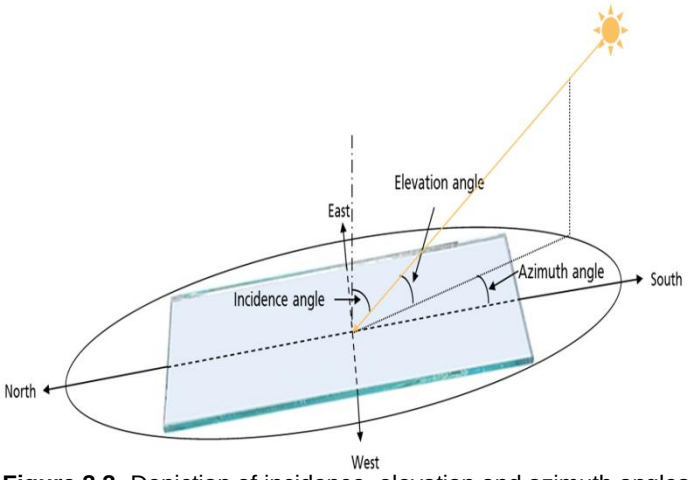

Figure 3.3: Depiction of incidence, elevation and azimuth angles

For a flat glass if intensity of the rays remains constant along the azimuth angles, an optical study with varying elevation angles at a particular azimuth angle would be representative of the performance of the glass for all the azimuth angles. A FEM study is carried out for six elevation angles starting from 90° to 15° with a step size of 15°. The geometry of the model consists of the glass structure and air medium; rays are released from the air medium onto the glass surface.

3.3 Results and discussion

A FEM based optical study is carried out for different elevation angles. Simulation results showing transmittance of glass for the different elevation angles are shown in table 3.3 and plotted in figure 3.4. The simulation results are compared with the theoretically calculated transmittance values which are obtained from equations (2.4-2.13).

Elevation angle (°)	**Simulation results: transmittance (W/m^2)**	**Theoretically calculated transmittance (W/m^2)**	**Difference (%)**
90	937.04	936.98	0.006
75	936.66	936.60	0.006
60	934.31	934.25	0.006
45	924.21	924.14	0.008
30	884.09	884.01	0.009
15	722.94	722.87	0.010

Table 3.3: Comparison of glass transmittance values obtained from simulation and analytical methods

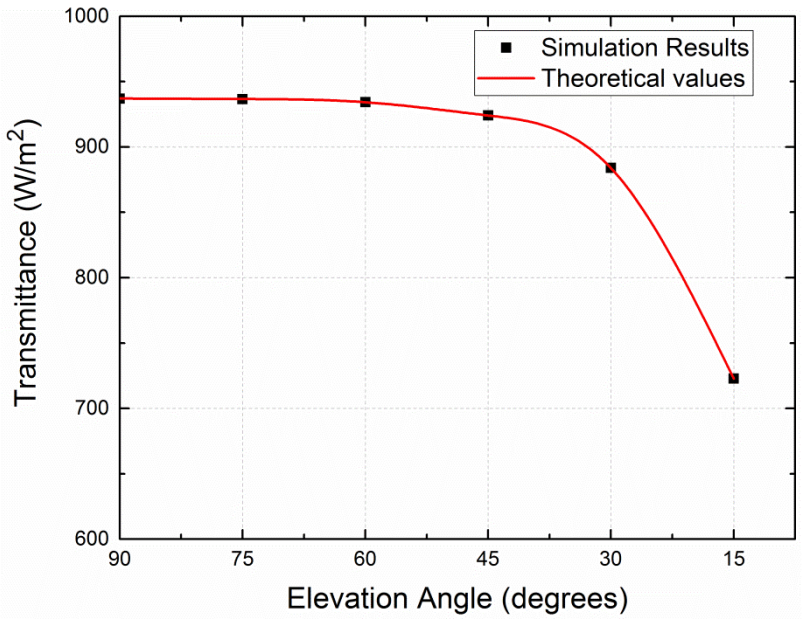

Figure 3.4: Comparison of glass transmittance values obtained from simulation and analytical methods

A very good agreement is obtained between the simulation results and the theoretical values as can be seen from figure 3.4. For all angles considered in the study, the error between the values is less than 0.01%. This good accuracy allows using the ray tracing tool for more complex systems

Solar rays incident on the air-glass interface looses energy due to reflections back to the air medium and absorption in the glass layer (Green, et al., 1995) [8]. For normal incident irradiance, this loss corresponds to 6.3% for a 3.2 mm thick low-iron soda lime glass. The reflection and absorption losses increase with decrease in the elevation angle, amounting upto 27% for an elevation angle of 15º. Another notable observation is that the irradiance loss for elevation angles in the range of 90º to 45º is almost constant.

Ray tracing and intensity variation of rays released from the air medium and falling at the air-glass interface at an elevation angle of 30º is shown in figure 3.5.

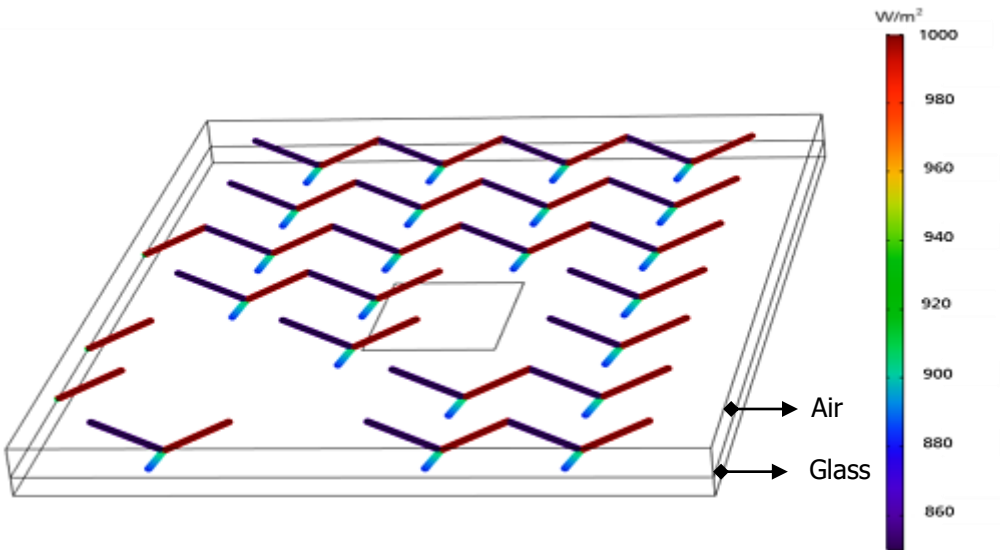

Figure 3.5: Simulation result showing rays incident on the glass medium from air at elevation angle of 30°; rays undergo reflection and refraction at the media interface according to Fresnel's equations

The figure above shows just a fraction (1%) of the rays (for clarity) that is incident on the glass surface. Incident rays of intensity 1000 W/m^2 (represented by red color in the legend spectrum) undergoes reflection (rays reflected back in the air medium represented by dark blue color) and refraction at the air-glass interface. Also, as rays travel further in the glass medium, their intensity reduces due to absorption loss (color changes from green to blue).

3.4 Improvement in transmittance

Due to an increase in the intensity of the reflected ray (Fresnel's equations), the transmittance at lower elevation angles decreases as we see in figure 3.4. This lowers the efficiency of the PV module when rays fall on it at lower elevation angles. This is typically the case for photovoltaic applications that are fixed and cannot orient according to the position of the sun. PV systems installed at roofs, walls of buildings, streets and pathways are a few such applications. In order to reduce the optical losses in PV modules (Duell and Ebert, 2010 [5]; Nositschka, 2008 [6]), effective design of the glass (structuring) can be applied. Another way to improve the transmittance is by the use of Anti-Reflecting (AR) coating on the glass surface which is not studied in this work to keep the models simple.

One example of glass structuring is the introduction of small pyramid-like structures on the front glass surface. The advantage of introducing such structures is to redirect the reflected ray on to the glass surface, thereby reducing the energy that is lost in the reflected ray.

3.4.1 Model designs (structure development)

To enhance the performance of glass at lower elevation angles following five models are developed and studied. They are shown in figure 3.6(a-e). For strength and stability of the modules, each model has a base glass of 2 mm thickness beneath the pyramid-like structures according to the minimum thickness of solar glass available in the market. The first glass model has conical-shaped pyramids whereas the other models have rectangular-shaped pyramids. For the models 1, 2 and 4, the flat, top plateau surface of the pyramids have an area which is 20 % of the base of the pyramid structure. For model types 3 and 5, the flat, top plateau surface of the pyramids has an area which is 40 % of the base of the pyramid structure.

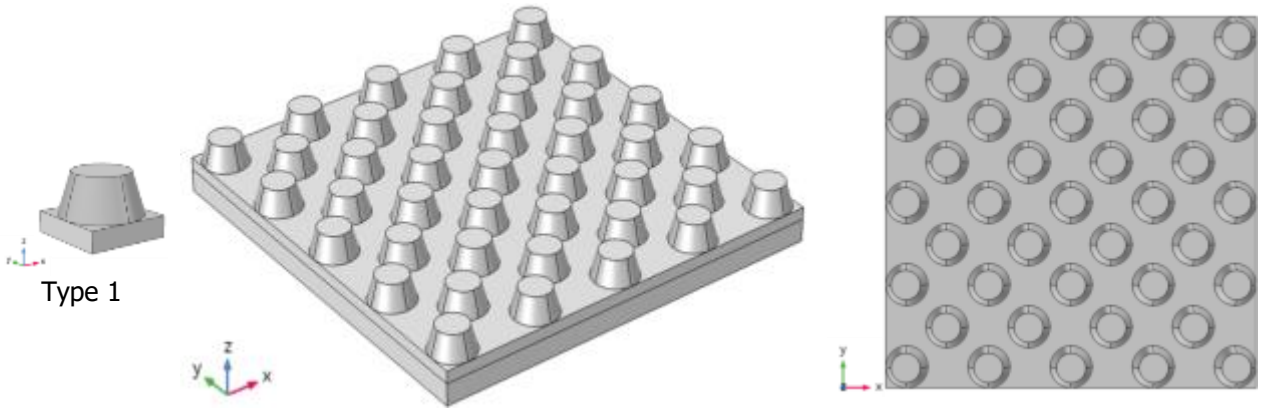

Figure 3.6(a): Type 1 glass design- conical shaped pyramid structures.

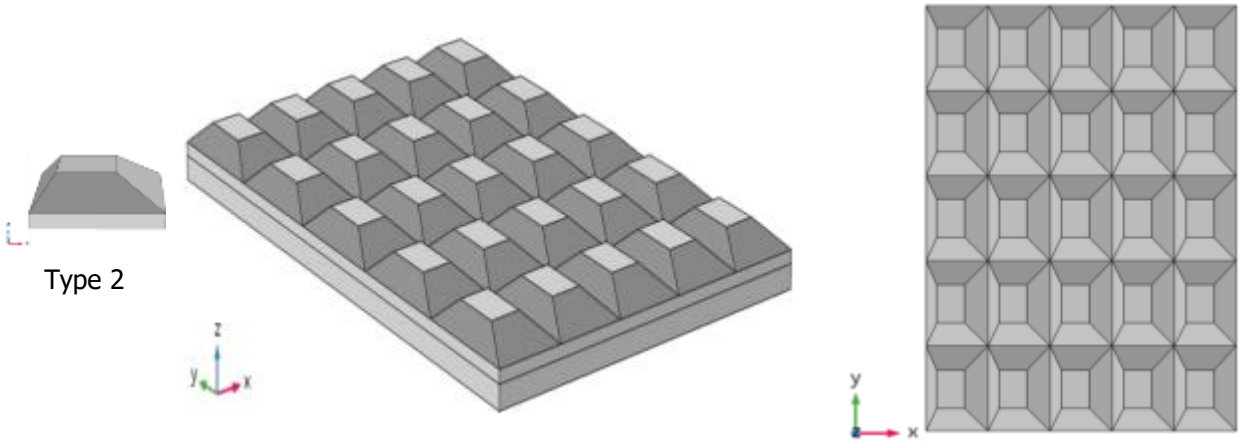

Figure 3.6 (b): Type 2 glass design- asymmetric pyramid structures: surface area of plateau is 20% of the base

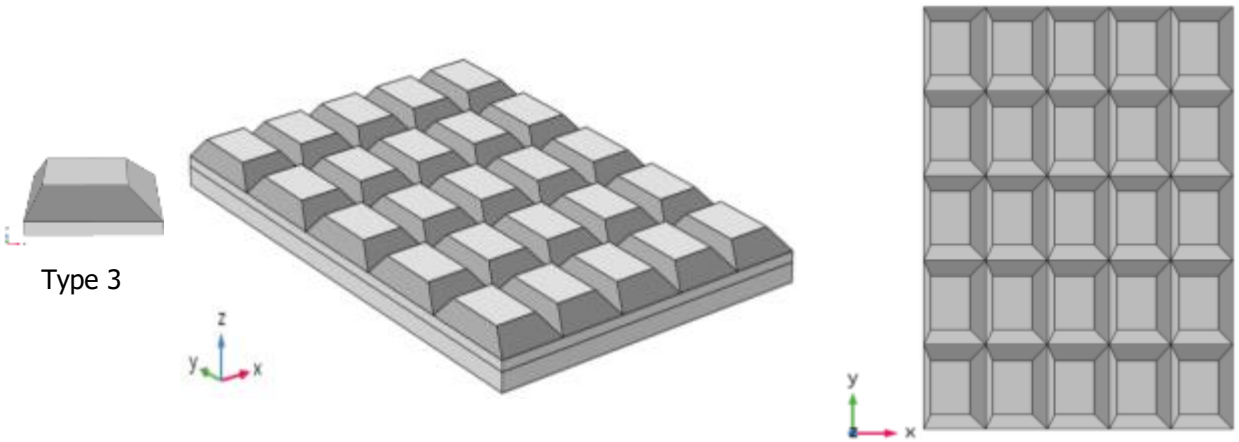

Figure 3.6 (c): Type 3 glass design- asymmetric pyramid structures: surface area of plateau is 40% of the base

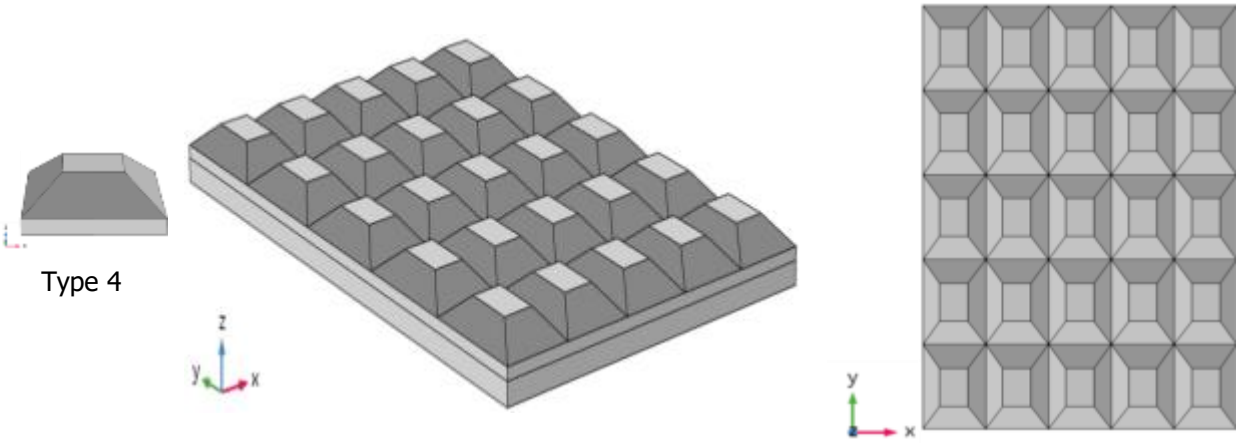

Figure 3.6 (d): Type 4 glass design- symmetric pyramid structures: surface area of plateau is 20% of the base

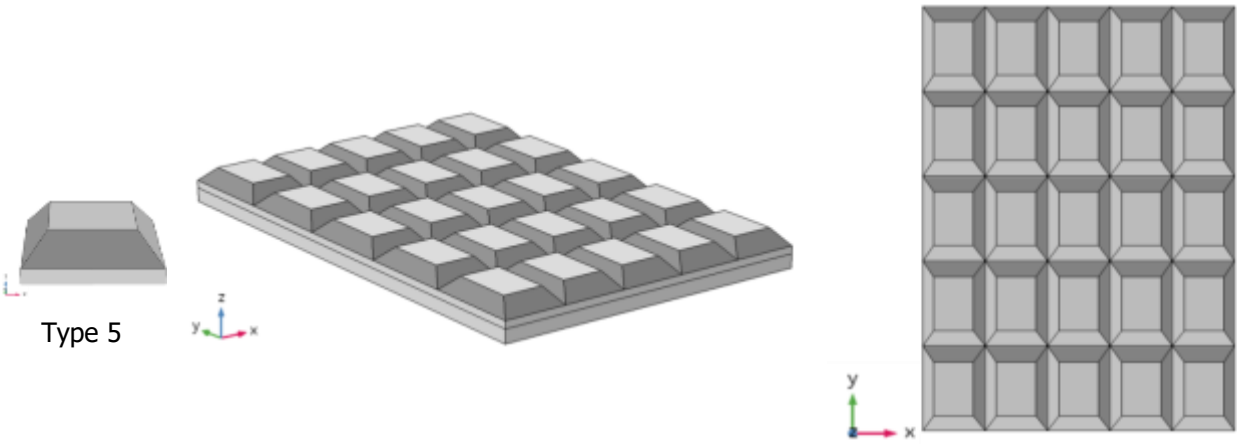

Figure 3.6 (e): Type 5 glass design- symmetric pyramid structures: surface area of plateau is 40% of the base

Figure 3.6 Different glass models studied. An isometric view and top view for each model type is shown

3.4.2 Assumptions and boundary conditions

The assumptions considered in the simulations to study the optical losses in the different structured glass models are the same as those assumed for the optical study of a flat glass slab. Unlike flat glass, the textured models have to be studied not just for the different elevation angles but also for different azimuth angles due to the 3-dimensional pyramid structure. The simulations are thus carried out for different elevation angles in the range of 90° to 15° and for different azimuth angles in the range of 0° to 180°.

3.4.3 Results and discussion

To compare the different angular behavior of the structures the transmitted energy is normalized to the normal incidence value.

The simulation results showing relative transmission intensity of the glass models for the different elevation and azimuth angles are depicted in figure 3.7.

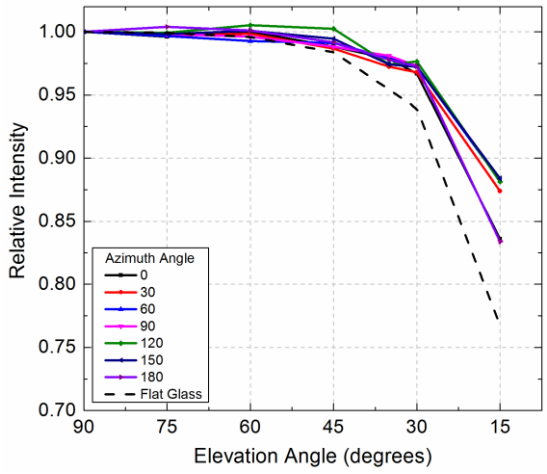

Type 1

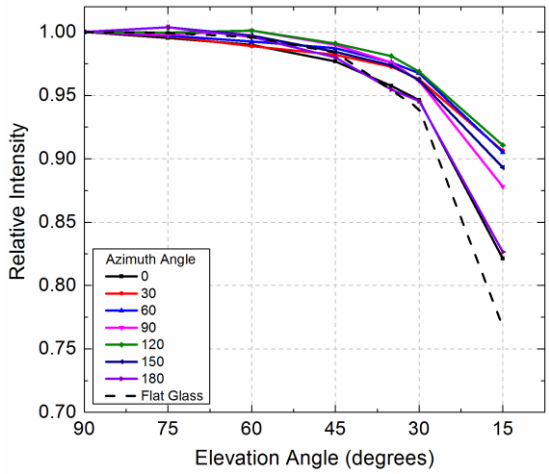

Type 2

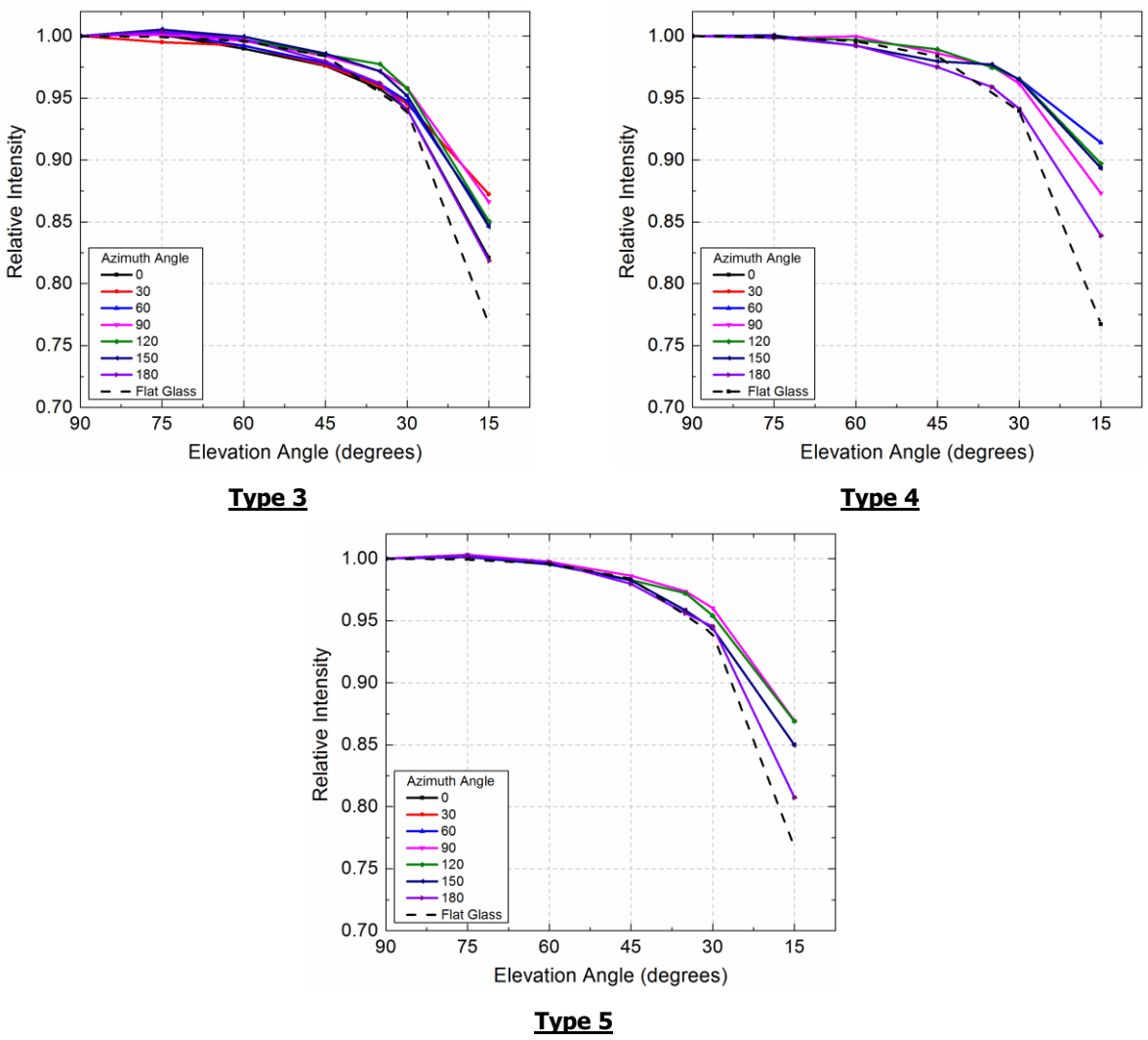

Figure 3.7: Transmittance computed in the 5 different structured glass models at different elevation and azimuth angles and their comparison to transmittance of flat glass

The advantage of introducing pyramid-like structures is easily demonstrated by the plots shown in figure 3.7. All the structured models in general reduce the optical losses when compared to losses of the flat glass. Unlike flat glass, these structured models have a varying performance over the range of azimuth angle. Since model types 4 and 5 are symmetric, the transmittance profile for symmetry angles overlap. For higher elevation angles there is not much difference in transmission (within 1-2%) between flat and structured glass models, however as the elevation angle decreases, a substantial improvement is noticed. From the simulation results, it can be seen that the transmittance at lower elevation angles (15º) for the different structured glass models is higher by 10-15% when compared to flat glass.

The reason for the increase in transmittance in structured glass is depicted in figure 3.8 which is obtained from the simulation; ray-tracing of two sets of rays, one falling on flat surface and the other on the sloped surface of pyramid structures can be seen.

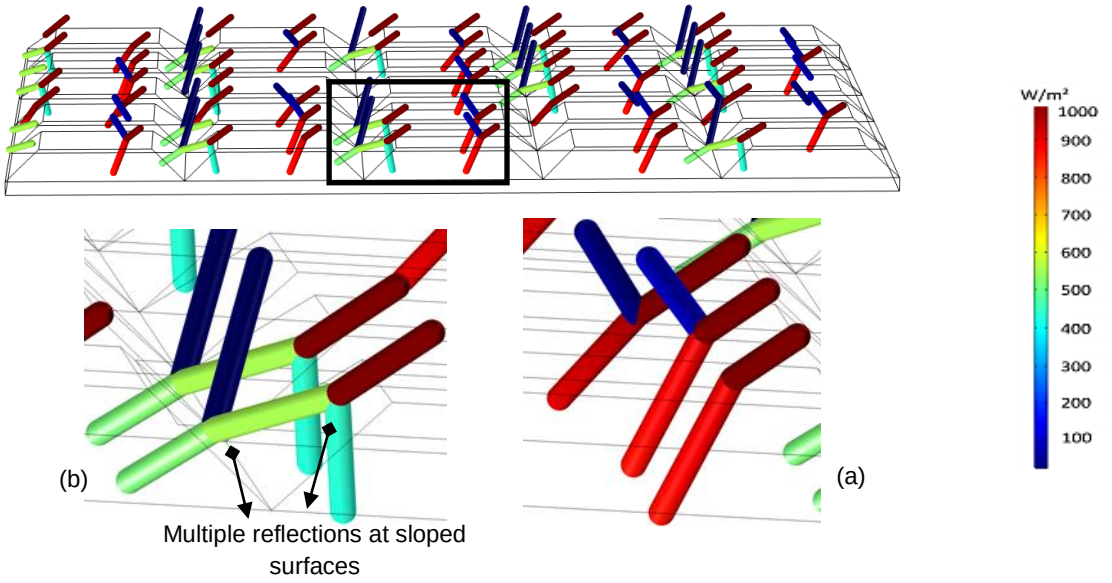

Figure 3.8: Tracing of rays falling on the type 5 glass design at elevation angle of 60º and azimuth angle of 60º at (a) flat plateau of the pyramids, (b) sloped sides of the pyramids; image obtained from simulation

Due to the presence of pyramid-like structures, the reflected ray is redirected onto the glass surface. The redirected ray is again both reflected and refracted at the glass interface. According to the color legend of the simulation result, the intensity of ray finally reflected back to the air medium for case (b) is lower than that for case (a).

The number of rays used in the simulation should be considerably high so that the results are accurate and have a fine resolution. In order to verify this, simulations with three different numbers of rays are carried out. The study is repeated for two different sets of elevation and azimuth angles. Figure 3.9 shows the simulation results displaying irradiance profile at the base of type 5 glass model when (a) 3000 rays, (b) 12000 rays and (c) 30000 rays are incident on the glass surface at (I) elevation angle=90º, azimuth angle=0º and (II) elevation angle=30º, azimuth angle=30º.

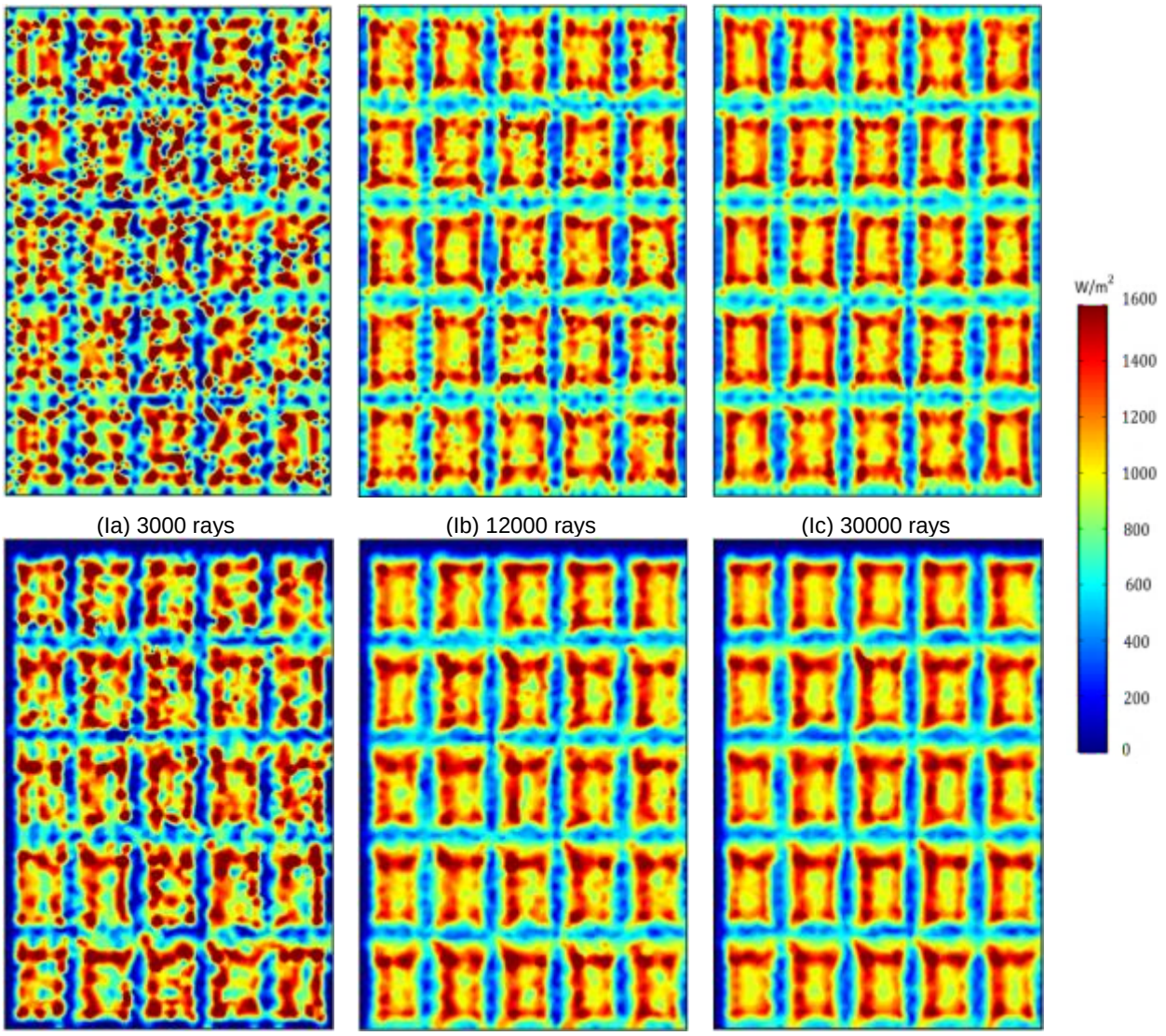

(Ia) 3000 rays (Ib) 12000 rays (Ic) 30000 rays

(IIa) 3000 rays (IIb) 12000 rays (IIc) 30000 rays

Figure 3.9: Simulation results showing irradiance profile at the base of type 5 glass when (a) 3000 rays, (b) 12000 rays, and (c) 30000 rays are incident on the glass surface at (I) Elevation angle=90º, Azimuth angle=0º and (II) Elevation angle=30º, Azimuth angle=60º

We can see from figure 3.9 that as the number of ray increases, the results have less noise. The irradiance distribution differs for the two different elevation and azimuth angles simulated, which will also be the case for other incident angles.

3.5 Optical study to compute ribbon shadow loss

Structuring the glass surface has another desirable effect. Due to the pyramid structures, the rays falling on the sloped surfaces are directed in the glass medium in such a manner that the cell area between the pyramids receives lower irradiance. From this result we suggest to place the busbars/ribbon interconnections of the solar cell in a lower irradiated area, which will studied below. Krauter, 1993 [33], demonstrated the effect of optical reduction of the inactive cell areas such as ribbons, pointing out that shadowing loss due to the ribbons is reduced by 70% due to structuring.

This phenomenon can be observed in figure 3.9. According to the colour legend of the simulation results, the irradiance between the pyramids is much lower compared to other areas. From this result we suggest to place the busbars/ribbon interconnections of the solar cell in a lower irradiated area, which will be studied below. To realize this, the optical study is extended to include the solar cell with busbars/ribbons and EVA layer on top of the cell (figure 3.10). A standard flat glass module of same dimensions is also studied in order to evaluate the effect of structured glass on the busbar/ribbon shadow loss.

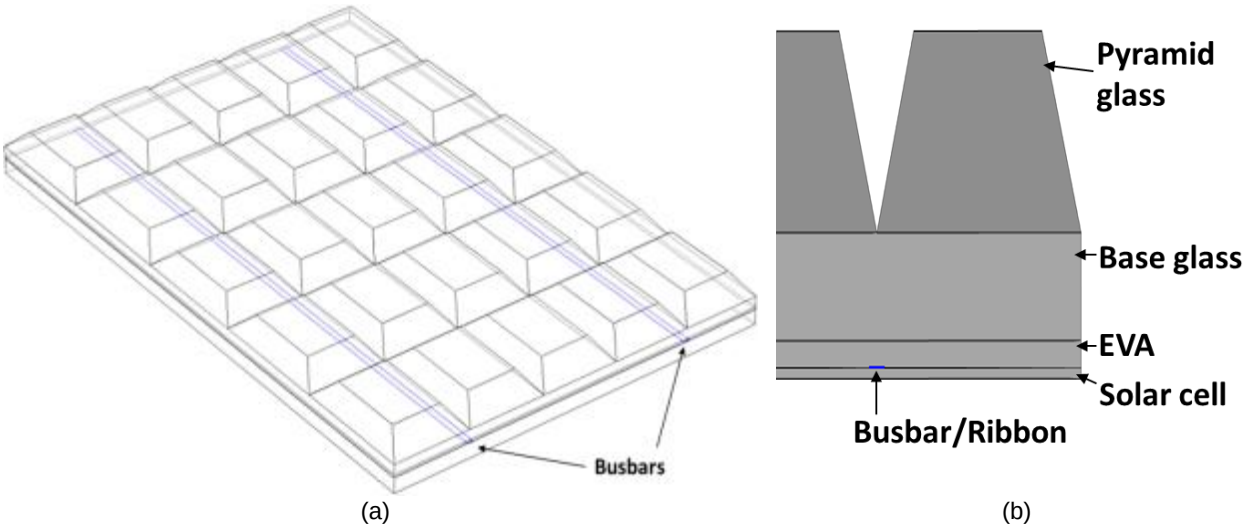

Figure 3.10: Module with busbar/ribbons placed under the groove of glass pyramid structures
(a) isometric view of the model (b) side view of the structure showing location of busbar

FEM optical study is now carried out on the models to calculate the irradiance reaching the solar cell. Optical properties of EVA, solar cell, and metallization are given in Appendix A. Since the illumination distribution in a structured-glass module for different incidence and azimuth angles has a similar pattern, the optical study to observe the busbar/ribbon shadow loss is limited to only the normal incidence. The other assumptions and boundary conditions of the simulations remain the same as in the simulation that was used to generate the irradiance profile in the type 5 glass model. Now, in addition to the losses in the

glass medium, reflection and absorption also takes place in the EVA and busbars/ribbons before reaching the cell. Results of the simulation are shown are shown in table 3.4

	Irradiance at cell level for a standard flat glass module (W/m^2)	**Irradiance at cell level for a module with type 5 glass design (W/m^2)**
Cell without busbar/ribbon	934.99	934.32
Cell with busbar/ribbon	908.50	933.30
Relative difference (%)	**2.83%**	**0.11%**

Table3.4: Comparison of irradiance of the solar cell in a standard flat glass module and in a module with type 5 glass model

The irradiance of the solar cell without any metallization for the two cases is seen to be almost the same (Table 3.4) for a normal incidence (elevation angle 90°). For a standard flat glass module, the illumination is uniform over the cell surface and so the shadow loss due to busbars/ribbons is directly proportional to the homogeneous irradiance. Shading loss due to busbars/ribbons in a standard flat glass module is computed to be 2.83% of the irradiance on cell. For a module with structured glass the irradiance is non-uniform over the cell surface. Rays are concentrated away from the region under the grooves of the pyramids in a structured glass module. When ribbons are placed over the cell in such a way that they lay vertically below the grooves of the glass pyramids, the shadow losses due to busbars/ribbon decrease substantially. Shading loss due to busbars/ribbons in a structured glass module is computed to be 0.11% of the irradiance on cell.

In the first part of the chapter the ray tracing tool is used to simulate a simple flat glass slab, transmittance of which can be easily calculated from analytical methods. A maximum error of 0.01% between the simulation results and the theoretical values demonstrate the precision of the tool, which is then used to simulate complex models designed to improve the transmittance of glass. Five different glass models are simulated under the same assumptions as those used for the flat glass. For lower elevation angles, the proposed pyramid-structured glass models were seen to have higher transmittance (an increase in transmittance of 10-15% at low elevation angles of 15°) when compared to flat glass. Further with the help of simulations, it was shown that the inhomogeneity in illumination introduced by the pyramid structures of the proposed glass models can be used to reduce the overall busbar/ribbon shadow loss from 2.8% of cell irradiance to 0.11%.

4 THERMAL MODEL

Efficiency of a photovoltaic module is inversely proportional to the operating cell temperature (Green, 1982) [8]. Further, the temperature gradient over a PV module introduces thermal stresses within the module (Lee, Y., et. al. 2012) [11]. Hence, in order to predict the performance of a PV module it is important to determine the cell temperature. Temperature in different layers is estimated by considering the thermal energy exchanges that takes place between the module and the environment.

Many FEM studies (Zhou, et al., 2015 [9]; Usama Siddiqui, et al., 2012 [10]; Lee, Y., et. al. 2012 [11]) have been conducted to simulate and analyze the temperature distribution in PV modules. All of these studies determine the heat absorbed in the different module components based on constant optical coefficients (reflectance, transmittance and absorbance). These coefficients however vary significantly with the irradiance incidence angle. For instance the reflection coefficient of glass can vary in a range of 0.04 to 1. In the model presented absorption of solar energy in the materials is measured with the help of ray optics tool, which allows analysis for any incidence angle. The attenuation in energy of solar rays as they are absorbed in the different materials is calculated from the optical study. Thus using a multiphysics simulation, heat absorbed in the module components can be accurately calculated by optical simulation and used as input for thermal study of PV modules.

4.1 Model description and nomenclature:

A one-cell PV module shown in figure 4.1 is simulated in this section to calculate the temperature distribution in the module. The three-dimensional model studied consists of the flat front glass cover, EVA encapsulating the solar cell and the Tedlar backsheet. To reduce the complexity of the simulation, metallization of the solar cell is not modeled. The solar cell has a dimension of 156 mm by 156 mm and the dimension of the module is 200 mm by 200 mm.

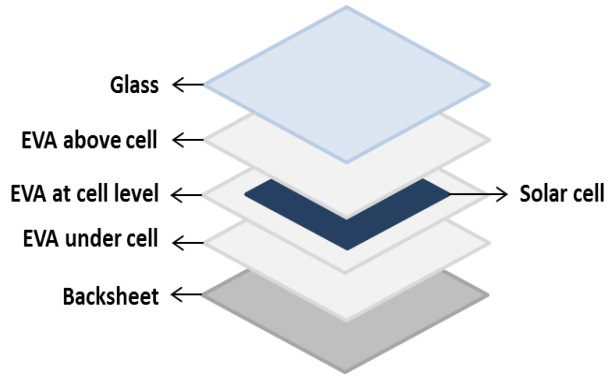

Figure 4.1: Components (not to scale) of a one-cell PV module used in the thermal simulation

Material properties of the components used in the simulation are given in Appendix A.

4.2 Assumptions of the simulation

The assumptions considered in the coupled optical and thermal simulations are shown in table 4.1.

Parameters	**Values**
Intensity of rays	1000 W/m^2
Wavelength of rays	750 nm
Elevation angle	90 degrees
Ambient temperature	293.15 K
Wind velocity	1 m/s
Front surface convective coefficient	9.89 $Wm^{-2}K^{-1}$
Rear surface convective coefficient	4.95 $Wm^{-2}K^{-1}$

Table 4.1: Assumptions of the coupled optical and thermal simulation of a one-cell PV module

- All material properties are considered isotropic and independent of temperature.
- Ohmic heating in the solar cells is considered negligible.
- The front and rear surface of the PV module is assumed to face the sky and ground respectively. Schott, 1985, found that the sky and ground temperatures can be assumed to be equal to the ambient temperature.
- The rear surface of the PV module is usually not as well cooled as the front surface, hence the convective heat transfer of the back surface is considered half that of the front (Lee, Y., et. al. 2012) [11].
- Steady state conditions are assumed.

Heat exchanges via convection and radiation are assumed to take place only from the front glass surface and Tedlar back surface. The convective heat transfer coefficient for the front surface is given by the equation 4.1 (Notton, et al., 2005) [24]

$$h = 5.82 + 4.07\, v \qquad (4.1)$$

where the wind speed is given by v (in meters per second).

A wind speed of 1 m/s which corresponds to wind speed for Nominal Operating Cell Temperature (NOCT) conditions is used in the simulations to calculate the heat-transfer coefficient. For the rear surface the coefficient is taken to be half that of the front surface [11]. Thus for the simulation heat transfer coefficients for the front and the rear surface are 9.89 W/m^2K and 4.945 W/m^2K respectively.

4.3 Results and discussion

FEM optical study of the model shown in figure 4.1 is performed to calculate the energy absorbed in the different module components and is shown in table 4.2.

Material	Heat Absorbed (kW/m^3)
Glass	9.14
EVA layer above cell	5.21
Silicon cell	4670
EVA layer at cell level	7.57
EVA layer under cell	2.96
Backsheet	2.80

Table 4.2: Heat absorbed in each material of the PV module; values are calculated using optical study of the model

Absorption of solar energy by the cell increases its temperature which decreases the electrical efficiency of PV modules (Skoplaki and Palyvos, 2009) [3]. The efficiency relation is given by equation 2.3.

The thermal study is iterated based on equation 2.3 until the efficiency and the cell temperature converges to a reasonable extent (difference between current solution and next iteration solution is less than 0.1%). Thermal profile of the module is shown in figure 4.2.

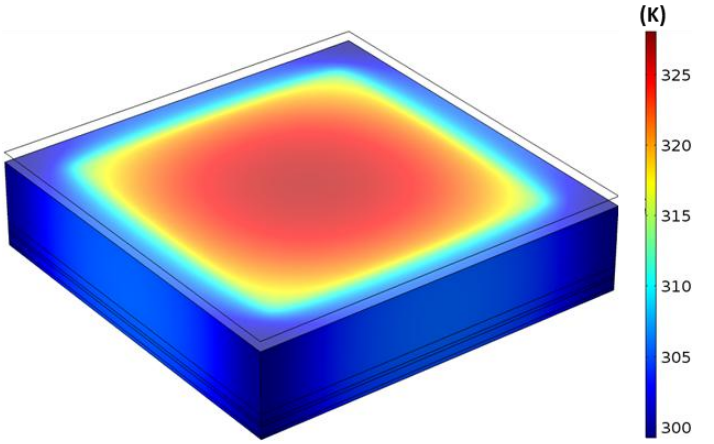

Figure 4.2(a): Thermal profile of the PV module; results obtained from coupled optical and thermal study

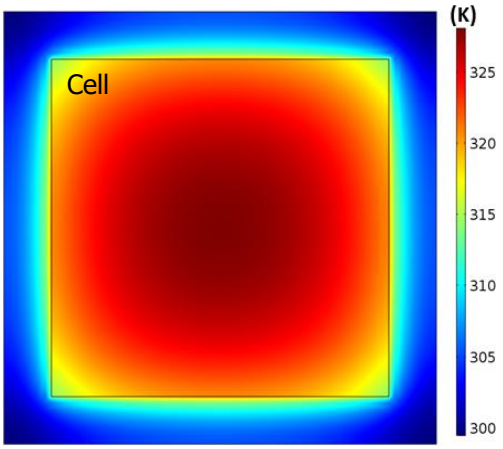

Figure 4.2(b): Thermal profile of the cell surface

Due to increase in the cell temperature the electrical efficiency decreases and final efficiency is calculated to be 15.57%. As the solar cell has a high absorption coefficient, solar energy is trapped more in the cell

than in the other components, which leads to a higher temperature of the cell. Temperature distribution in the thickness of the PV module at the center, cell edge and cell corner is shown in figure 4.3.

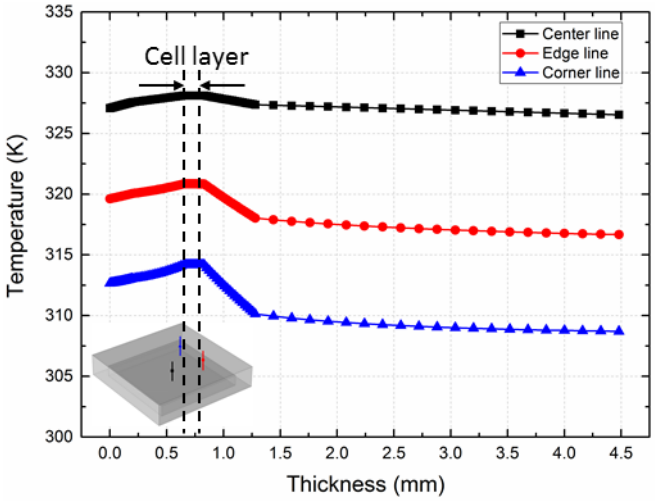

Figure 4.3: Multiphysics simulation result showing the temperature distribution in the thickness of the PV module at center, cell edge and cell corner of the model under study

For all the three lines considered, the temperature increases along the backsheet and the rear EVA layer, reaches a maximum at the cell layer and then decreases in the upper layers. The maximum temperature difference between any two points in the thickness of the module along the three lines is calculated and given in table 4.3.

	Maximum Temperature (K)	Minimum Temperature (K)	Max. Temperature Difference (K)
Cell center	328.1	326.5	1.6
Cell edge	321.3	316.9	4.4
Cell corner	314.1	308.2	5.9

Table 4.3: Analysis of temperature distribution at the different points in the thickness of simulated model

At the cell center, the temperature is almost uniform and the maximum temperature difference is 1.6 K. However, temperature difference increases at the cell edge and cell corner. This temperature gradient over a PV module induces thermal stresses within the module (Lee, Y., et. al. 2012) [11]. The temperature distribution of the solar cell layer's central cross-section is plotted in figure 4.4.

From Figure 4.4 shown below, we see that the highest temperature of the cell is 328 K and is located at the center of the cell. Cell temperatures decrease with distance from the cell-center; however the temperature distribution pattern remains the same.

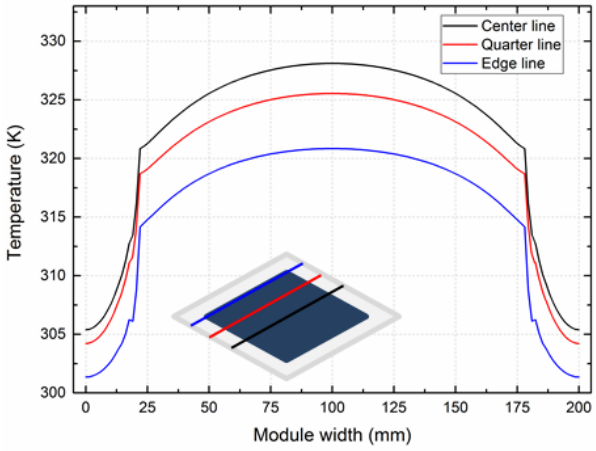

Figure 4.4: Temperature distribution of the solar cell layer's central cross-section for a flat glass PV module

The effect of changes in material or boundary conditions of the model can be easily evaluated in FEM simulations. The environmental conditions play a crucial role in the heat exchange and thus influence the cell efficiency and the resulting power output. The cell efficiency increases as the difference between the cell temperature and the reference temperature (ΔT) decreases according to equation (2.3). Among the various external conditions that influence the energy output, the effect of ambient temperature and wind speed are studied. To analyze this dependence, thermal simulations are carried out for different ambient temperature in the range of 0°C to 40°C in intervals of 10°C, and wind velocity in the range of 0 to 10 m/s in steps of 2 m/s is simulated.

Changes in efficiency due to variation of ambient temperature (T_{amb}) and wind velocity (v) for a uniform solar irradiation of 1000 W/m^2 is shown in figure 4.5.

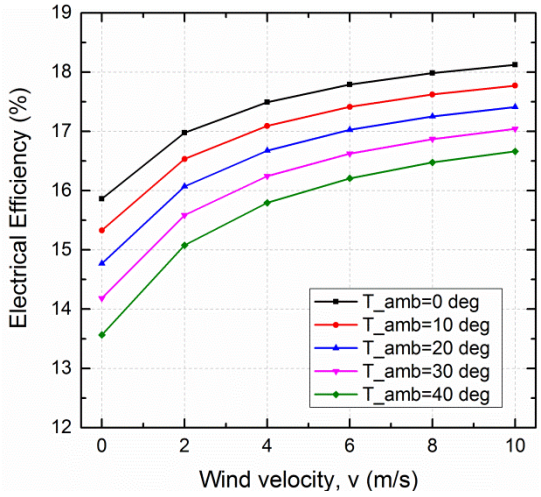

Figure 4.5: Influence of ambient temperature and wind velocity on electrical efficiency of the model studied

In the graph 4.5 above, each line represents a fixed ambient temperature and the efficiency is plotted against the wind velocity, v which varies from 0 to 10 m/s. As expected, one can see from figure 4.5 that the cell efficiency increases with decrease in ambient temperature and increase in the wind velocity. Higher wind velocity ensures a better convective heat transfer from the module surfaces thereby lowering the cell temperature. For a particular ambient temperature, say for an ambient temperature of 20^{o}C, the efficiency changes from 14.8% at a wind velocity of 0 m/s to 17.4% at a wind velocity of 10 m/s. This corresponds to a relative efficiency difference of 13.7%. A lower ambient temperature causes a better heat exchange with the surroundings. For a constant wind speed of 2 m/s, the efficiency changes from 17.0% at ambient temperature of 0^{o}C to 15.1% at ambient temperature of 40^{o}C. This corresponds to a relative efficiency difference of 12.6%.

4.4 Thermal modeling for inhomogeneous irradiance

Most of the studies conducted so far to analyze the temperature distribution in a PV module using finite element method (Zhou, et al., 2015 [9]; Usama Siddiqui, et al., 2012 [10]; Lee, Y., et. al. 2012 [11]) are based on homogeneous irradiation. Solar cells however operate under non-uniform illumination in certain situations such as in concentrated and bifacial PV, during partial shading of the module, or when structured glass is used in the module instead of flat glass. In these cases, a model based on a combination of optical and thermal physical phenomena can calculate the heat absorbed in the different module components with a much finer resolution than the earlier models where heat sources are determined analytically based on constant optical coefficients and homogeneous irradiance. Such a multiphysics model enables analysis of systems with a higher degree of accuracy.

In this section temperature distribution in a module with inhomogeneous illumination is studied and the scope of multiphysics study is exhibited. For the study, a model of a PV module with type 5 structured-glass shown in figure 21 is studied. From optical simulations carried out in chapter 3.4 we have seen that the irradiance pattern on the solar cell in a structured glass module is non-homogeneous. Figure 4.6 shows irradiance of a cell in a type 5 structured glass module simulated for an elevation angle of 90^{o} (normal incidence) and 30000 number of rays.

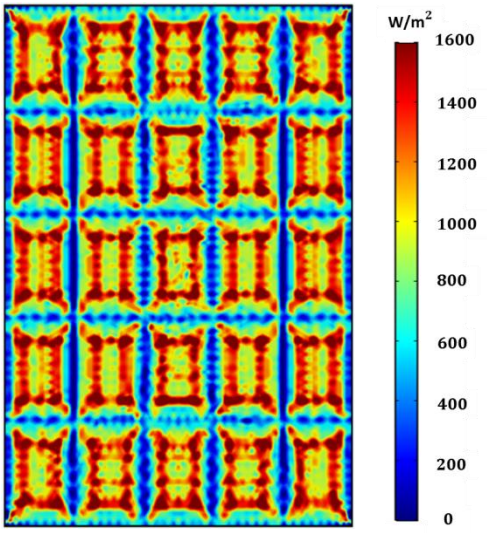

Figure 4.6: Optical simulation result showing the irradiance profile of a cell in a type 5 structured glass module simulated for an elevation angle of 90° and 30000 number of rays

Along with the cell, the other module components also will have distributed and non-uniform energy absorption. The absorption of solar energy in each of the different layers is evaluated from the optical study of the model, which is then used to compute the temperature profile in the module.

A thermal study of the module with structured glass (type 5 model) on top is carried out using the assumptions and boundary conditions stated in table 4.1. The simulation result displaying the temperature profile of the model under study can be seen in figure 4.7.

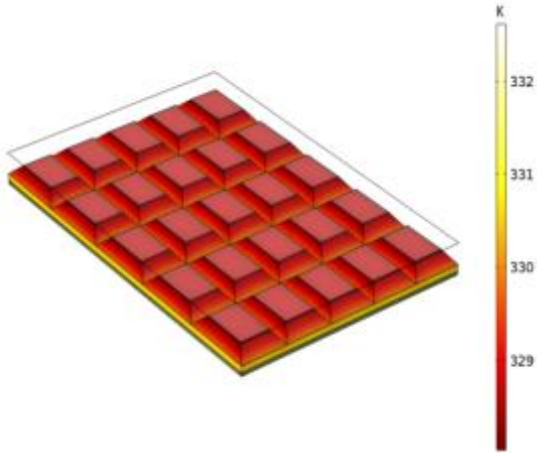

Figure 4.7(a): Thermal profile of module with type 5 structured glass; profile obtained from coupled optical and thermal simulation

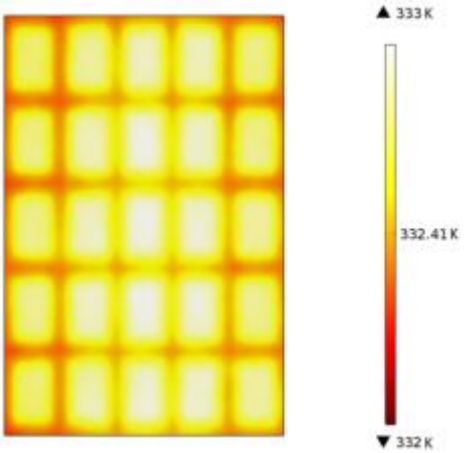

Figure 4.7(b): Thermal profile of cell surface of the simulated model

The effect of inhomogeneous illumination can be seen on the thermal profile. The temperature distribution at the solar cell layer's central cross-section is shown in figure 4.8. Thermal profile of the PV module is obtained from coupled optical and thermal study. The gradient from left to right is an academical result with the simulation precision. The scale is kept small to illustrate the temperature fluctuations.

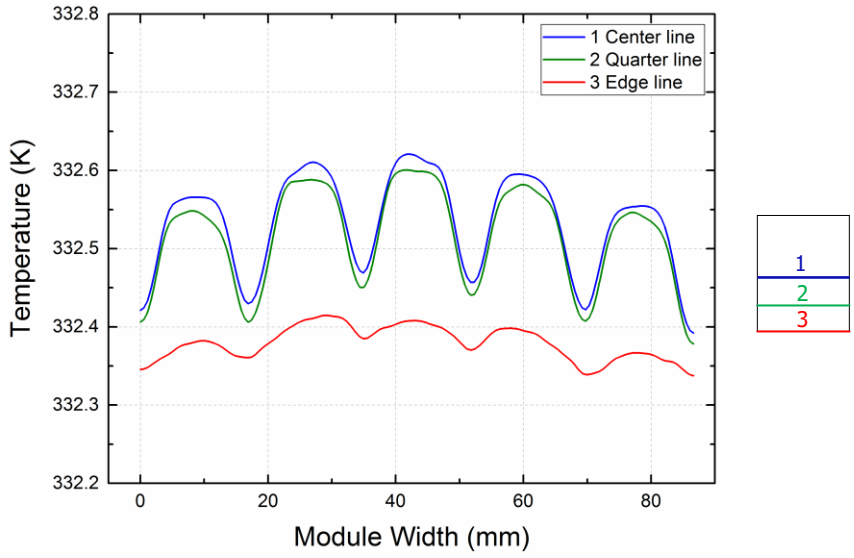

Figure 4.8: Temperature distribution of the solar cell layer's central cross-section for a structured PV glass module

Temperature in the solar cell layer is highest at the center and then decreases while moving towards the edge as also seen for the cell in a flat glass module. However, unlike a single curved temperature profile along the width of the cell obtained for a flat glass module (figure 4.4), the profile along the width of the cell in a structured glass PV module has many bell-shaped curves (figure 4.8). This is due to fact that the rays falling on the glass are directed by the glass pyramids and form an irradiance pattern shown in figure 4.6, thereby concentrating the heat source on the solar cell in the higher irradiance parts. We can thus see from here the importance and relevance of a multiphysics study to investigate the behavior of the system under study.

5 ELECTRICAL MODEL

Current generated in the solar cell pass from the rear metallized surface, vertically through the bulk to the emitter where it flows laterally into the finger, from the finger to the busbar and finally into the interconnecting ribbon from the busbar (Franklin, et al., 2002) [25]. The total series resistance of the cell is given by the sum of all the individual component resistances. Power losses in contact resistances and base resistance are typically much smaller than those in the emitter and metallization (Haas, et al., 2014) [27] and thus have been neglected for the simulations in this work. A significant power loss and reduction in open-circuit voltage due to the thin high-sheet resistance emitter layer is reported by many studies (Smirnov, et al., 1980 [28]; Mitchell, 1977 [29]; Franklin, et al., 2002 [25]). A non-uniform illumination augments the loss [27]. In this chapter, power loss in emitter layer of the solar cells is studied for both uniform and non-uniform illumination using finite element electrical analysis.

A simple 3-D model consisting of the base, emitter layer and two adjacent fingers is first simulated. The study is repeated by varying the cell parameters. For such a simple model, it is easy to compute the ohmic loss from analytical methods. The simulation results are compared to theoretical solutions obtained from eq. 2.28 to validate the simulation approach which is later used in the study of complex models.

5.1 Simulation of a simple 3-D model

5.1.1 Model description and nomenclature:

A cell cross-section with two metal fingers and a half-width busbar as shown in figure 5.1 is modeled for the study.

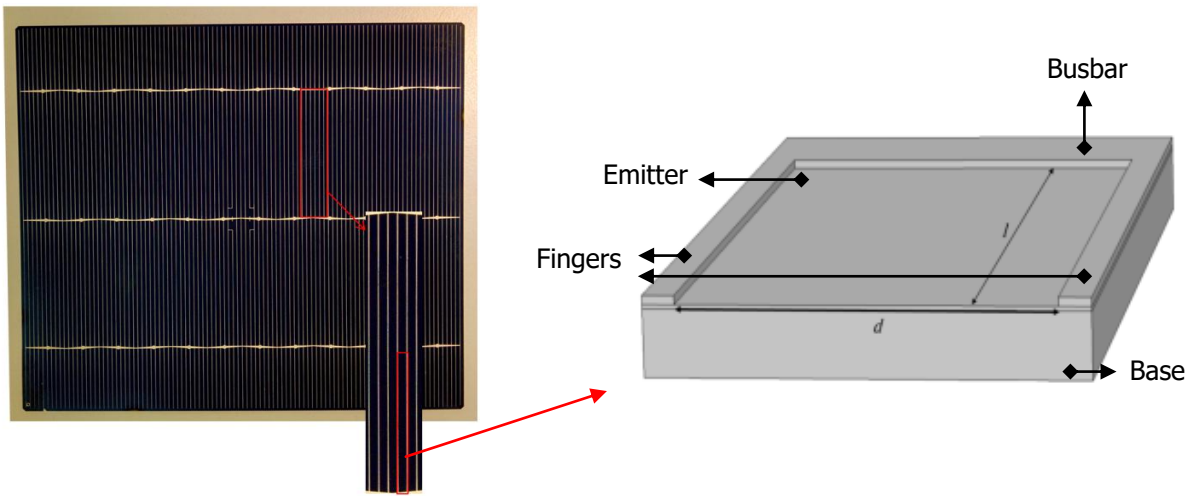

Figure 5.1: Model of cell cross-section simulated to calculate power loss

The ohmic loss in the shallow emitter region depends on four parameters (eq. 2.28): length of the fingers given by l, the distance between the fingers d_f, current density J, and emitter sheet resistivity ρ_e. In the 3-busbar solar cell shown above, the adjacent busbars/ribbons are separated by a distance of 52 mm and the distance between adjacent fingers (d_f) is 1.46 mm. Even though ohmic loss due to emitter resistance only is computed in this work, losses can be calculated for any individual series resistance component or for the entire cell.

5.1.2 Assumptions and boundary conditions for the simulation:

To carry out the FEM electrical study, the materials are considered to be homogeneous and the material properties independent of temperature.

Parameters	**Values**
Emitter sheet resistivity, ρ_e	71 Ω/sq (Fellmeth, et al., 2014) [34]
Current density, J	35 mA/cm^2 (Kim H., et al., 2013) [35]

Table 5.1: Assumptions for electrical simulation of cell cross-section shown in figure 5.1

- The emitter region is assumed to be uniformly doped.
- Irradiance is assumed to be uniform and same for the different simulation cases.

5.1.3 Simulation results for the simple 3-D model

The model is simulated to compute power loss in the emitter for different finger spacing (d_f). The results are cumulated in table 5.2:

Finger spacing d_f *(mm)*	**Simulation result: emitter power loss (mW)**	**Theoretically evaluated emitter power loss (mW)**	**Error (%)**
1	$1.89*10^{-2}$	$1.89*10^{-2}$	**0.32**
1.25	$3.69*10^{-2}$	$3.68*10^{-2}$	**0.24**
1.5	$6.37*10^{-2}$	$6.36*10^{-2}$	**0.20**
1.75	$1.01*10^{-1}$	$1.01*10^{-1}$	**0.18**
2	$1.51*10^{-1}$	$1.51*10^{-1}$	**0.14**

Table 5.2: Comparison of simulation results and analytical solutions of the emitter power loss of cell cross-section shown in figure 5.1

The power loss in emitter computed from the simulations shown in Table 5.2 is in agreement with the solutions obtained from eq. 2.28 (error between the values is less than 0.32%). For the specified assumptions and boundary condition, the simulation generates a current flow in the cell model as shown in the figure 5.2 below:

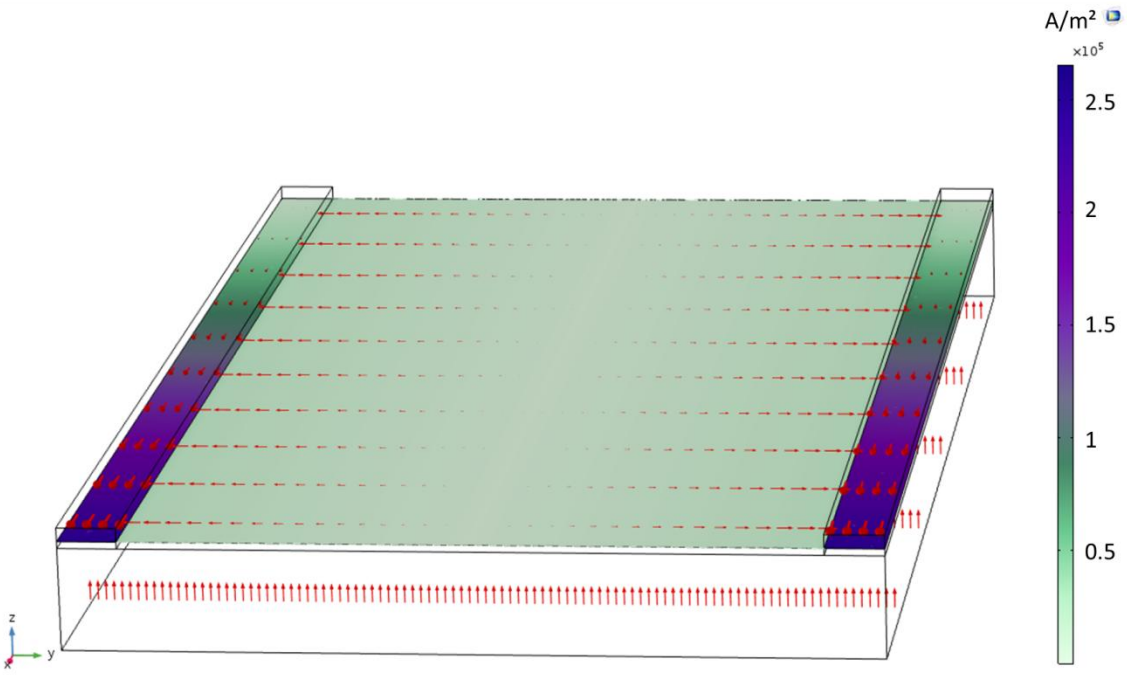

Figure 5.2: FEM simulation result showing the current flow in the cell cross-section

Conforming to the theory, current flows vertically in the bulk region, and laterally in the shallow emitter region into the metal fingers.

The accuracy of the simulation results compared to the analytical solutions in the case of a simple model with homogeneous illumination allows using a similar approach to perform simulations with inhomogeneous illuminations which are difficult to analyze analytically.

5.2 Simulation of cells with inhomogeneous illumination

Bifacial solar cells and concentrated PV cells have an inhomogeneous cell illumination during their operation. This inhomogeneity mostly resembles a gaussian distribution (Johnston, 1998) [12] as can be seen in the illumination profile of an installed concentrated PV module (figure 5.3).

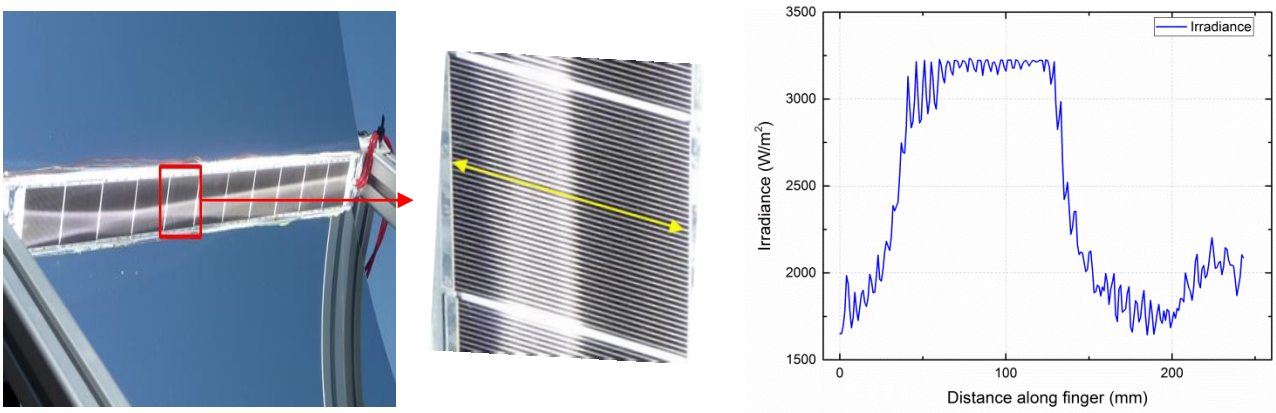

(a) CPV system (b) Solar cell (c) Cell irradiance in finger direction

Figure 5.3: Non-uniform illumination profile of an installed concentrated PV (CPV) solar module

The figure above shows inhomogeneity (irradiance varies from 1650 W/m^2 to 3226 W/m^2) in the finger direction. However, non-uniformity may also exist in the busbar direction (Coventry, 2005) [36], which will be studied here. Some parts of the cell receive higher irradiance as compared to the others. Due to this inhomogeneity, current generation in the cell will also be non-uniform. Ohmic loss is strongly dependent on the current density. For a cell with uniformly distributed finger grid and operating under inhomogeneous irradiance, ohmic losses increase when compared to cell operation under uniform illumination of same average irradiance. Increasing the total number of fingers (decreasing the spacing between fingers for the entire cell) will reduce the ohmic losses, but will also increase the finger shading loss [34]. Using FEM based electrical simulation, optimization of the grid can be carried out such that the finger spacing at a cell region is dependent on the irradiance. To observe emitter power loss in a spatially varying irradiance profile, a grid with non-uniform finger spacing is analyzed for a hypothetical gaussian distribution.

5.2.1 Model design

A solar cell having dimensions of 10 cm by 10 cm and with two busbars is assumed to have a gaussian illumination profile as can be seen in the figure 5.4. The gaussian profile has a peak value of 1600 W/m^2 (1.6 times the average value) and a minimum value of 246 W/m^2 (0.246 times the average value). Due to symmetry in the pattern, the model can be reduced to a quarter of the cell (5 cm by 5 cm) in order to reduce the complexity and the computing time and resources.

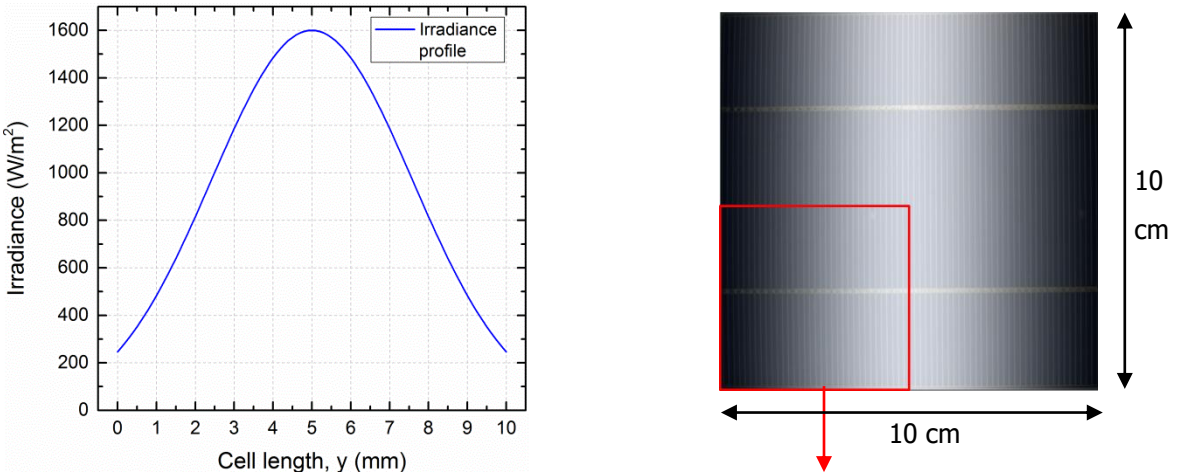

(a)

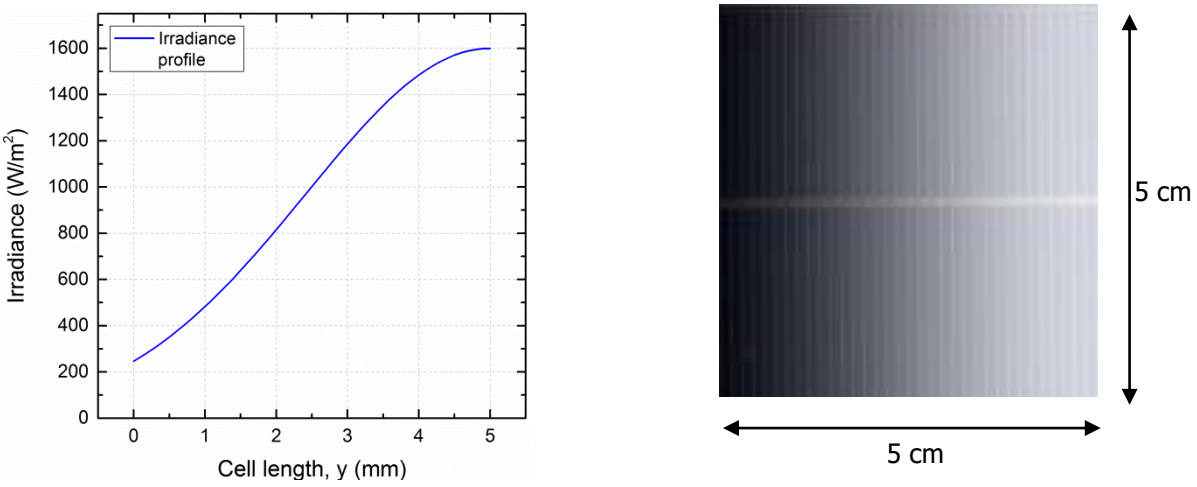

(b)

Figure 5.4: (a) (Right) A two-busbar solar cell under gaussian irradiance (left) **(b)** (Right) Symmetrical quarter cell-part of the two-busbar solar cell under gaussian irradiance (left)

The quarter cell-part modelled has a total of 32 fingers, each with a width of 85 µm and a busbar with a width of 1.5 mm. The finger grid proposed and studied is non-uniformly distributed over the cell surface and is divided into 8 segments, each segment having 4 fingers. Distance between the alternate fingers in each segment is constant and is a function of the illumination. Finger distances in the 8 segments so formed are in the range of 1.15 mm to 1.85 mm; fingers in the segment that receives the highest illumination are separated by the lowest distance and vice versa as shown in figure 5.5a. In order to evaluate the result, another model with the same number of fingers but uniformly distributed and cell receiving the same illumination profile is also studied. The fingers in this model are separated by a distance of 1.59 mm between alternate fingers as shown in figure 5.5b.

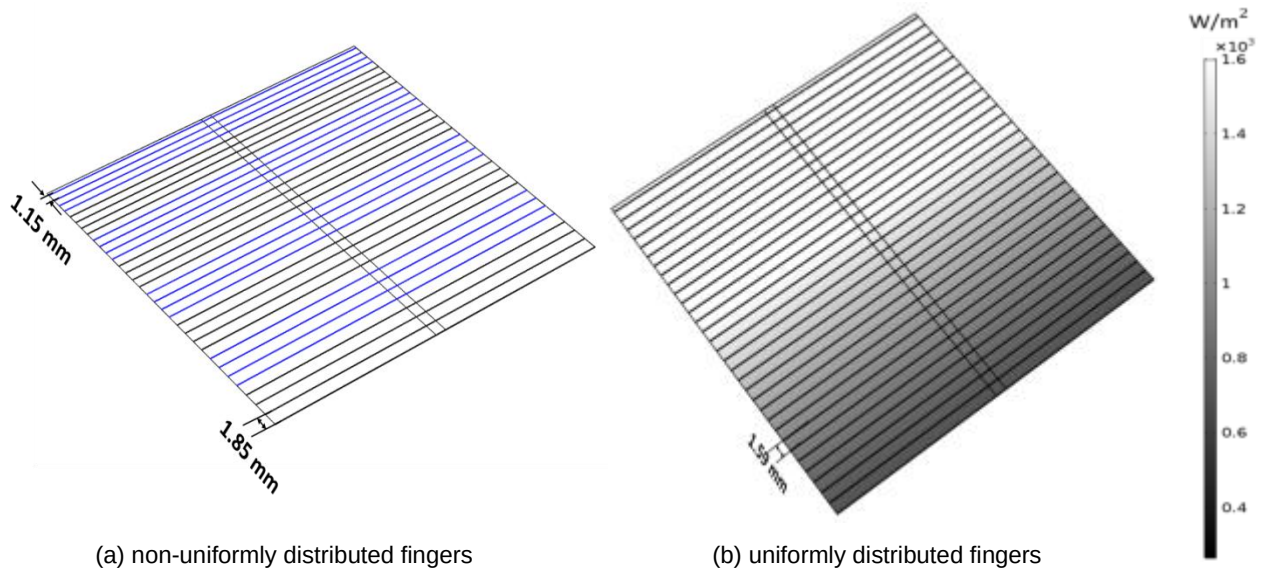

(a) non-uniformly distributed fingers (b) uniformly distributed fingers

Figure 5.5: Modeled quarter cell-part with **(a)** non-uniformly distributed fingers **(b)** uniformly distributed fingers. In the non-uniform grid, alternate finger segments are colored. In each segment, finger spacing is kept constant.

The model is finely meshed into very small elements (figure 5.6) which though increases computing time also produces accurate result.

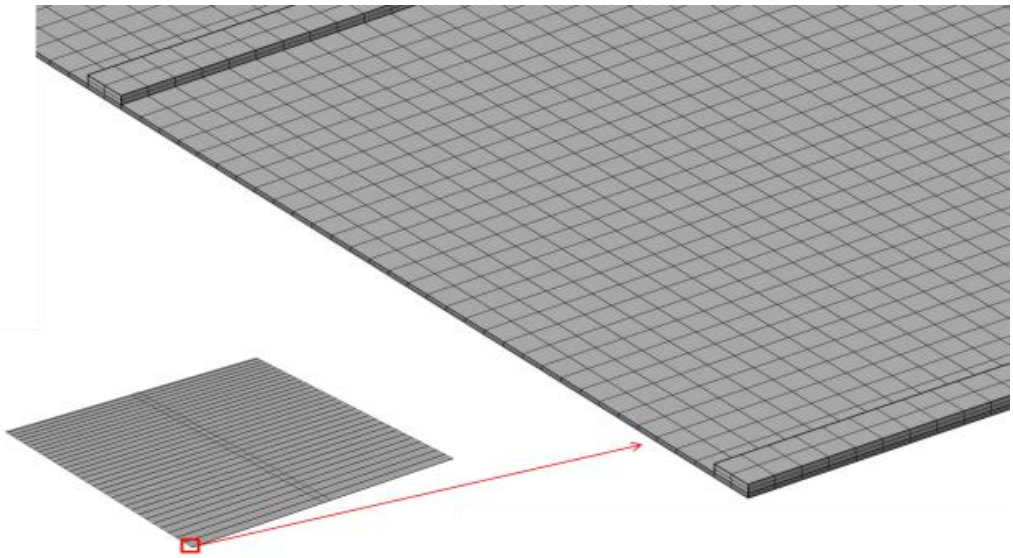

Figure 5.6: Meshing employed on the modeled cell-part (figure 5.5) in order to carry out the FEM study

5.2.2 Assumptions of the simulations

The gaussian irradiance distribution used in the simulation is attained using equation 5.1 [25]:

$$I_{irr} = I_{peak} e^{-\frac{y^2}{2\sigma_{sd}^2}} \tag{5.1}$$

where I_{peak} is the highest irradiance value in the distribution

σ_{sd} is the standard deviation of the distribution

y is the distance from the center of the cell

Parameters	Values
Peak irradiance	1600 W/m^2
Average irradiance	1000 W/m^2
Standard deviation of Gaussian distribution, σ_{sd}	2.5845 cm
Emitter sheet resistivity, ρ_e	71 Ω/sq (Fellmeth, et al., 2014) [34]
Current density, J	35 mA/cm^2 (Kim H., et al., 2013) [35]

Table 5.3: Assumptions for electrical simulation of a quarter cell model under gaussian irradiance distribution

Current generated at a localized part of the solar cell is proportional to the irradiance falling on that part. Current density, J (in mA/cm^2) generated at a particular point in the cell due to the irradiance, I (in W/m^2) is given by equation 5.2[1]:

$$J = \frac{I}{1000} * 35 \tag{5.2}$$

With these assumptions and boundary conditions, a FEM study is executed for the two models.

5.2.3 Results and discussion

A steady-state FEM study is conducted on the two models to compute the emitter power loss due to the gaussian illumination pattern. Due to different grid patterns in the two models, the shading loss due to the metallization also differs. Table 5.4 compares the emitter power loss and the average irradiance in the two models.

[1] Current density of 35 mA/cm^2 is obtained when the cell operates under an irradiance of 1000 W/m^2 (STC conditions) [35]

	Emitter power loss (mW)	Average irradiance (W/m^2)
Cell with non-uniformly-distributed finger grid	3.75	914
Cell with uniformly-distributed finger grid	4.39	917
Relative difference	**17.1%**	**0.33%**

Table 5.4: Simulation results showing the emitter power loss and average irradiance in both the models studied under the hypothetical gaussian irradiance

We can clearly see from the simulation results that emitter power loss of a cell with non-uniformly distributed metal grid is relatively lower than that of a cell with uniformly distributed metal grid. Average irradiance received by the cell having a non-uniform grid is lower than that of cell with uniform grid due to the fact that finger shading increases in the former case. In this study the non-uniform finger grid was divided into segments, finger spacing varies in different segments however distance between alternate fingers in each segment is constant. Optimization of the study is possible by further reducing the segment size. The current flow established at the emitter surface, fingers and the busbar is shown in figure 5.7.

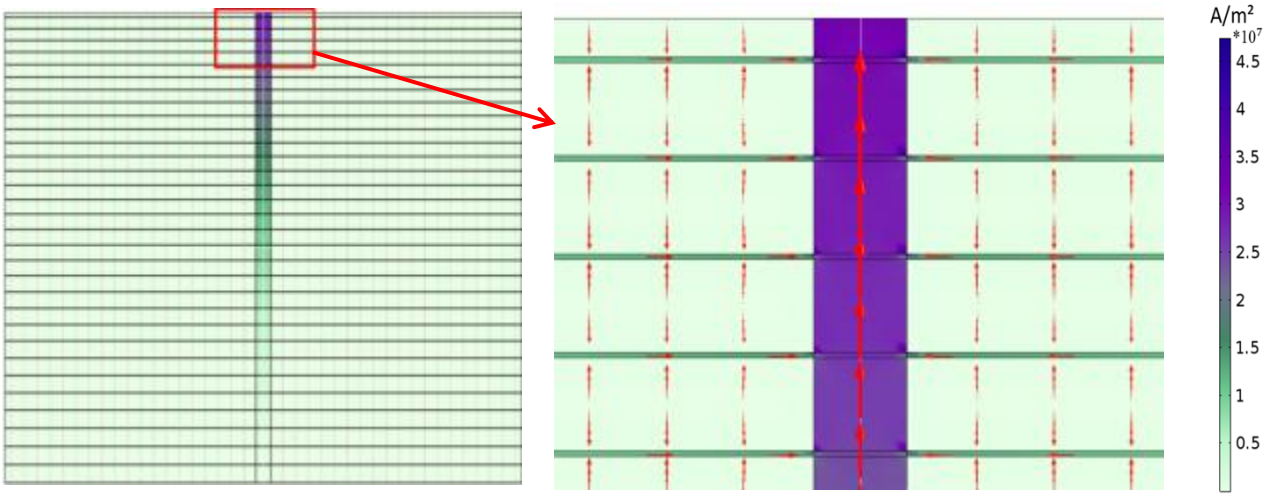

Figure 5.7: Simulation result showing the current flow at the emitter surface, fingers and busbar for a cell-part with non-uniform finger grid

The model designed to calculate the emitter power loss is working as desired and can be coupled with other physical phenomena to study real world situations.

5.3 Coupled optical and electrical study of structured-glass modules

The irradiance of a cell (without metallization) in a structured glass module (type 5) calculated earlier for an elevation angle of 90° with the help of optical simulation is shown in figure 5.8:

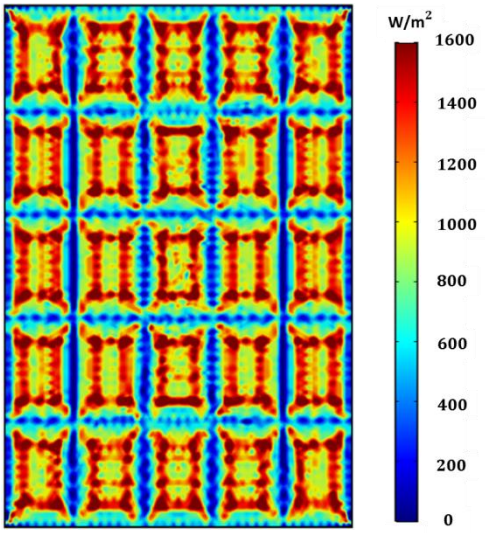

Figure 5.8: Optical simulation result showing irradiance of a cell in a type 5 structured glass module for an elevation angle of 90°.

With the help of the legend of the simulation result, we can see that the irradiance in cell parts under flat pyramid areas is higher than the irradiance in the parts under the pyramid grooves. In this section, the effect of placing the fingers closely in the higher illumination region on both emitter power loss and shading loss is studied with the help of combined optical and electrical simulations. Thus, a coupled optical and electrical study is carried out here to test and optimize a new design.

Two different finger spacing are used to create the grid; a smaller spacing between fingers is used in higher illuminated regions that are under the flat plateau area of the pyramids. To compare the model, another grid with an equal number of fingers but with fingers uniformly distributed over the cell is also simulated. The two finger grid models evaluated are shown in figure 5.9. First an optical study of the two models is simulated to generate the cell irradiance profile. Due to different arrangement of fingers in the two models the irradiance also differs. The cell irradiance obtained from the optical study of the models is then used in the electrical simulation to calculate the power loss in the emitters. Even though ohmic loss due to emitter resistance only is computed in this work, electrical losses can be calculated for any individual series resistance component or for the entire cell using multiphysics simulations.

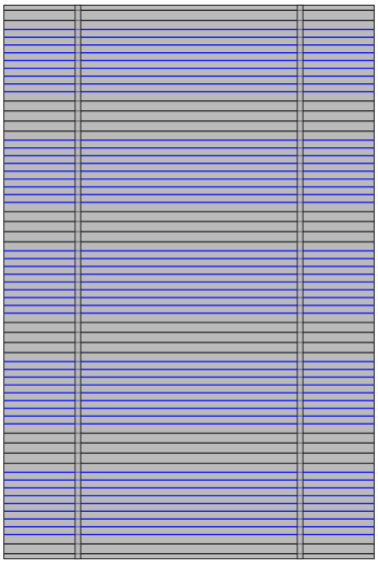

(a) non-uniform finger grid

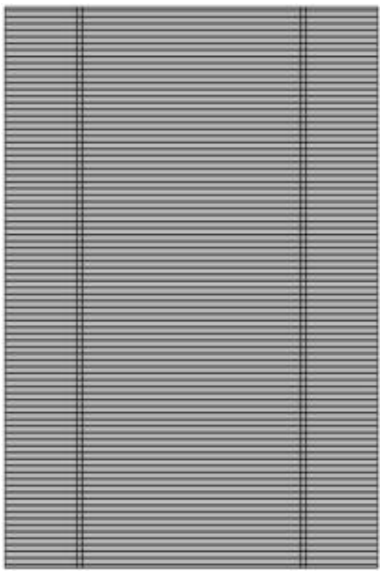

(b) uniform finger grid

Figure 5.9: Top view of cells modeled for type 5 structured-glass module with **(a)** non-uniform finger grid **(b)** uniform finger grid. Closely spaced fingers are represented in blue color in the non-uniform grid.

The combined optical and electrical simulations give the emitter power loss and average irradiance of the solar cells with the different finger grids and are shown in table 5.5.

	Emitter power loss (mW)	**Average irradiance (W/m^2)**
Cell with non-uniformly-distributed finger grid	3.78	880.94
Cell with uniformly-distributed finger grid	3.90	881.37
Relative difference	**3.17%**	**0.05%**

Table 5.5: Simulation results showing the emitter power loss and average irradiance in the two models studied

Emitter power loss and average irradiance of the solar cell with a non-uniform finger grid is marginally lower than for the cell with uniform grid. Effect of a lower irradiance due to higher finger shadow loss in the modified grid reduces the improvement attained by a reduction in the emitter power loss. With the help of the electrical simulation results of gaussian illumination irradiance and irradiance pattern obtained due to a structured glass, we can conclude that although an inhomogeneously illuminated cell with a non-uniform grid has lower emitter loss, it also has a lower average irradiance. Therefore for bifacial solar cells, low concentrated PV and structured-glass modules which have inhomogeneous illumination, the low power gain would not legitimate potential higher production costs for custom metallization.

6 EXPERIMENTAL VERIFICATION

This section details the outdoor experiments carried out on a one-cell PV module and multiphysics study of the PV module to validate the accuracy of FEM simulations. Since most part of the thesis is based on simulations, it is important to demonstrate their accuracy in modeling real world situations.

6.1 Experimental set-up

The experiments were conducted outdoors at Fraunhofer ISE with the objective of generating thermal profile on the solar cell with different illumination patterns. The module was constructed with the components as shown in the figure 6.1:

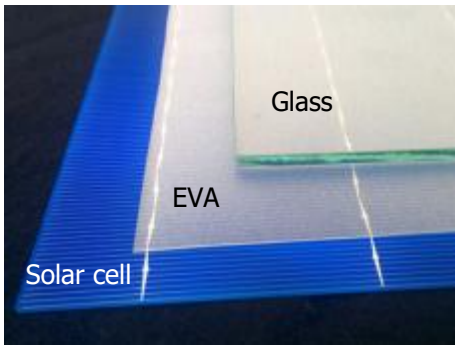

Figure 6.1: Components (solar cell, EVA and glass) used to prepare the module used for the outdoor experimentation

All the solar energy absorbed by the cell in the module is converted into thermal energy as the cell is not electrically connected and in open circuit mode. Since a thermal profile of the solar cell is desired which is measured with an Infrared (IR) camera, the back (or non-sunny) side of the solar cell is not covered with EVA or backsheet layers. The experimental set-up is shown in the figure 6.2 below.

An aluminum profile is used to keep the IR-camera aligned with the mini-module and at a fixed focal distance. The aluminum beam profile is placed in such a way that the elevation angle of the solar cell is close to 90º. The camera is set to capture the temperature profile of the back side of the solar cell repeatedly at a frequency of 1 second. The IR camera used has an accuracy of $\pm$ 2ºC for temperatures below 100 ºC [37]. Since EVA and solar cell constitute the back surface of the module, each having a different emissivity factor, the back surface was spray painted with black color to have a uniform emissivity. The emissivity of the back surface is calculated in a laboratory experiment and the value is found to be 0.95.

For an accurate assessment, the experiments were repeated for different illumination patterns. In order to create the illumination patterns on the solar cell, three different masks were employed. The aluminum masks were carefully aligned and kept at a separation of 5 mm from the front side of the module. These masks allow solar direct irradiation to reach the module top surface only through their openings thereby developing the desired illumination on the solar cell. Three different masks are used which are shown in figure 6.2:

(a) masks used to create different illumination profile on cell surface

(b) experimental set-up

Figure 6.2: (a) Different masks employed to create illumination patterns (masks numbered 1, 2, and 3 from left to right), **(b)** experimental set-up: a mask kept in front of the mini-module to create the desired illumination pattern on the solar cell

6.2 Experiment results

The temperature profiles of the solar cell rear surface captured by the IR camera for the three masks are shown in figure 6.3.

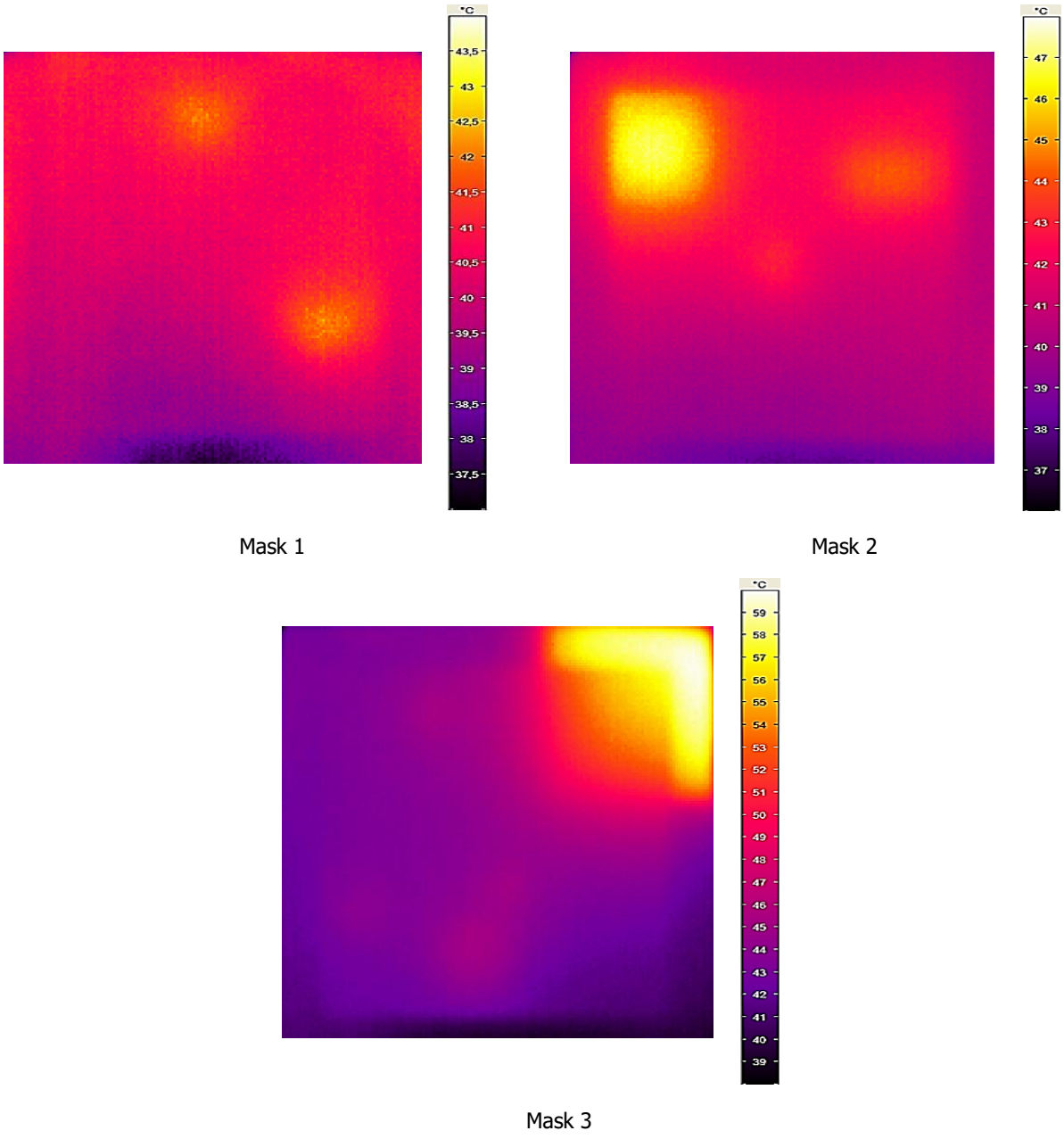

Figure 6.3: Experimental results showing the IR camera captured temperature profile of the solar cell rear surface

6.3 Multiphysics simulation

The experiment conducted on the PV-module involves a coupling of two physical processes, namely:

- Absorption of solar energy by the module,
- Heat dissipation from the module.

This experiment is then modeled in the FEM software to assess the accuracy of the simulations. Multiphysics study comprising 'Ray optics' and 'Heat transfer' physics modules are used in the simulations to represent the above mentioned processes.

With the different masks a known inhomogeneous illumination profile is generated on the module surface. The simulation is defined to include the optical losses in the different layers of the module. The energy absorbed by the components is set as heat source. Thus the output of the optical study is used as input for the thermal study. At steady state conditions, the thermal study creates a temperature profile of the module.

6.3.1 Assumptions of the simulation:

There are various factors that have to be accounted for in order to represent a real system as a computer model. It is extremely difficult to accurately predict the values of some of these factors. Taking appropriate assumptions in the simulation can reduce the complexity while producing fairly accurate results. The assumptions considered for the simulation are:

Parameters	Values
Wavelength of rays	750 nm
Absorption coefficient of solar cell	0.9 [9]
Reflection coefficient of solar cell	0.1 [9]

Table 6.1: Assumptions for multiphysics simulation study of a one-cell module

- All the media are homogeneous and have a uniform refractive index.
- The incident radiations are considered to be unpolarized in nature.
- All material properties are considered isotropic and independent of temperature.
- The top surface of the PV module is assumed to face the mask whereas the back surface is assumed to face the ground. The ground temperature is assumed to be equal to the ambient temperature (Schott, 1985) [38].
- The ambient conditions are taken to be constant during the experimentation.

6.3.2 Boundary conditions of the simulation:

A model can uniquely represent a system when appropriate input and boundary conditions are applied on the model. The boundary conditions that are imposed on the model in this simulation are as follows:

Parameters	Values
Global Horizontal Irradiance (GHI)[2]	810 W/m^2
Direct Normal Irradiance (DNI)[2]	740 W/m^2
Mean ambient temperature[2]	32.3 ºC
Mean wind velocity[2]	0.71 m/s
Emissivity of glass	0.85
Emissivity of back surface	0.95
Metal coverage area	0.07% of cell area

Table 6.2: Boundary conditions for multiphysics simulation study of a one-cell module

- The front metallization of the solar cell was not included in the study in order to reduce the complexity of the simulation. The solar energy lost due to presence of the fingers and busbars is however incorporated in the study by reducing the cell heat source by 7 percent.
- Emissivity of glass used was determined in a laboratory experiment and was found to be 0.85. The glass surface views the aluminum mask which gets heated under sun during the experiments. Since EVA and solar cell constitute the back surface of the module, each having a different emissivity factor, the back surface was spray painted with black color to have a uniform emissivity. The emissivity of the back surface is calculated in a laboratory experiment and the value is found to be 0.95.
- Given the wind velocity, convective heat-transfer coefficient is calculated from eq. 3.3. The top surface of the module is enclosed by the mask, thereby limiting forced convection from the glass surface. From eq. 3.3, heat-transfer coefficients for the top and back surface are given by 5.82 W/m^{2}K and 8.71 W/m^{2}K respectively.

6.4 Results and discussion

Using the assumptions and boundary conditions defined as above, a FEM model of the module is simulated. It is important to mention here that the assumptions and boundary conditions were unchanged for the multiphysics studies of the three different illumination patterns. The computed temperature profile of the solar cell back surface with the different masks is shown in figure 6.4.

[2] Conditions at Freiburg, Germany on 16th August, 2016 when the experiments were conducted. Values are obtained from Fraunhofer ISE's official weather station.

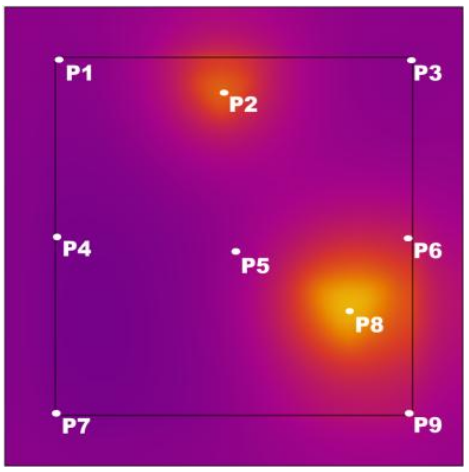

Figure 6.4(a): Mask 1 simulation result: temperature profile of the cell rear surface

	Experiment results (°C)	Simulation results (°C)	Absolute Temperature difference (°C
P1	40.7±2	39.6	1.1±2
P2	41.8±2	41.6	0.2±2
P3	40.8±2	39.7	1.1±2
P4	40.2±2	39.5	0.7±2
P5	40.2±2	39.8	0.4±2
P6	40.7±2	40.0	0.7±2
P7	39.5±2	39.5	0.0±2
P8	42.1±2	42.8	0.7±2
P9	39.7±2	40.3	0.6±2
Average over points	40.6±2	40.3	0.6±2

Table 6.3(a): Comparison of experiment and simulation results at points indicated in figure 6.4(a)

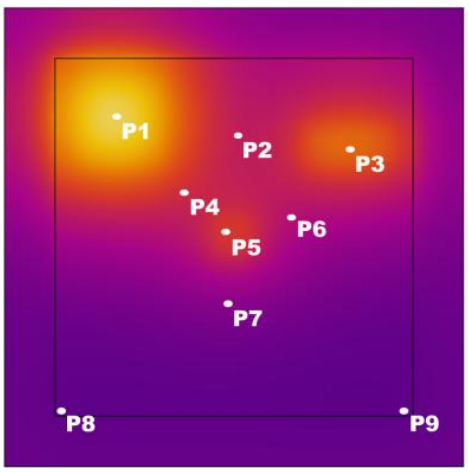

Figure 6.4(b): Mask 2 simulation result: temperature profile of the cell rear surface

	Experiment results (°C)	Simulation results (°C)	Absolute Temperature difference (°C)
P1	47.0±2	46.9	0.1±2
P2	42.6±2	42.0	0.6±2
P3	44.1±2	44.0	0.1±2
P4	42.6±2	42.4	0.2±2
P5	42.8±2	42.8	0.0±2
P6	41.9±2	41.8	0.1±2
P7	40.4±2	40.1	0.3±2
P8	39.4±2	39.8	0.4±2
P9	39.5±2	39.8	0.3±2
Average over points	42.3±2	42.2	0.2±2

Table 6.3(b): Comparison of experiment and simulation results at points indicated in figure 6.4(b)

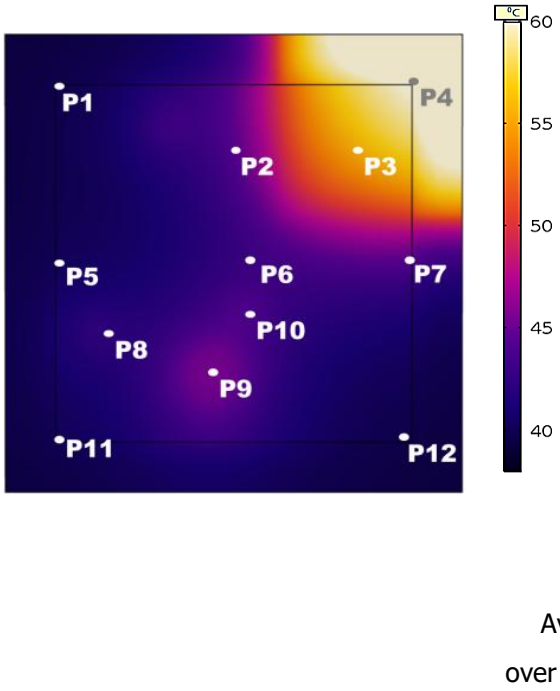

Figure 6.4(c): Mask 3 simulation result: temperature profile of the cell rear surface

	Experiment results (°C)	Simulation results (°C)	Absolute Temperature difference (°C)
P1	41.8±2	40.4	1.4±2
P2	45.8±2	44.6	1.2±2
P3	54.3±2	55.2	0.9±2
P4	59.4±2	60.2	0.8±2
P5	42.0±2	40.5	1.5±2
P6	44.1±2	43.6	0.5±2
P7	44.8±2	44.1	0.7±2
P8	43.3±2	42.6	0.7±2
P9	44.5±2	45.6	1.1±2
P10	44.4±2	44.2	0.2±2
P11	40.6±2	40.2	0.3±2
P12	39.5±2	39.9	0.4±2
Average over points	45.4±2	45.1	0.8±2

Table 6.3(c): Comparison of experiment and simulation results at points indicated in figure 6.4(c)

The temperatures at same points for the IR-camera images and simulation results for each mask demonstrate a good degree of correlation between the experiment and the simulation results. The average absolute temperature difference between experimental and simulation results is found to be 0.6±2°C.

7 CONCLUSIONS

The use of FEM multiphysics simulation tools to study PV modules is presented in this thesis. In the optical part, the ray tracing tool is used to simulate a simple flat glass slab. The result is compared to the analytically calculated values. A maximum error of 0.01% between the simulation results and the theoretical values demonstrate the precision of the tool, which is then used to simulate novel glass structures designed to improve the transmittance of glass. For lower elevation angles, the proposed pyramid-structured glass models were seen to have higher transmittance (an increase in transmittance of 10-15% at low elevation angles of 15°) when compared to flat glass. Further with the help of simulations, it is shown that the inhomogeneity in cell illumination caused by the structured glass can be used to reduce the overall busbar/ribbon shadow loss from 2.8% of cell irradiance to 0.11%.

A new multiphysics simulation model to analyze thermal behavior of PV modules is then proposed and evaluated. In this model the heat absorbed in the different module layers is obtained from the optical study. This multiphysics study model enables accurate analysis of PV modules operating under diverse conditions. In comparison to the earlier thermal models, the proposed model calculates the heat absorbed in the materials from an optical study which incorporates factors such as wavelength and incidence angle of the irradiance. A further advantage of such a combination of two physical models could be the implementation of temperature dependence of optical material properties.

In order to reduce ohmic losses in the emitter for an inhomogeneous illuminated solar cell, non-uniformly distributed finger grid is designed and modeled. A gaussian irradiance profile and an irradiance profile generated by a structured glass module are used for the electrical simulation. Using coupled optical and electrical simulatons, performance of the new grid models is investigated. From the multiphysics simulations one can see that although the emitter power loss is reduced in a non-uniform finger grid, the low power gain would not legitimate potential higher production costs for custom metallization. Here the potential of multiphysics study to analyze complex interacting models is demonstrated. Further inter-linking of the various physical phenomena (optical, thermal and electrical) is proposed for future work.

In the final part, outdoor experiments are carried out to validate the optical and thermal multiphysics simulations. The simulation and experiment are repeated for three different illumination patterns to test the performance of FEM multiphysics simulations. For the three study cases considered, the average temperature difference between experimental and simulation results is found to be 0.6 ± 2°C. The accuracy of the multiphysics simulation tool to model PV modules qualifies its use in the early stage of module development.

APPENDIX

	Glass	EVA	Solar cell	Backsheet
Refractive Index, η	1.518 [32]	1.487 [39]	3.723 [30]	1.46 [40]
Extinction coefficient, k	4.067E-7 [32]	1.34E-7 [39]	7.759E-3 [30]	2.98E-7 [41]
Thermal Conductivity (W/m K) [9]	2.00	0.311	130	0.15
Specific Heat Capacity (J/kg K) [9]	500	2090	677	1250
Density (kg m^{-3}) [9]	2450	950	2330	1200
Emissivity [9]	0.85	-	-	0.9

Table A: Material properties of the components used in the simulations

REFERENCES

[1] I. Haedrich, U. Eitner, M. Wiese and H. Wirth, “Unified methodology for determining CTM ratios: Systematic prediction of module power,” *Solar Energy Materials and Solar Cells,* vol. 131, pp. 14-23, 2014.

[2] “Trina Solar Annual Report, 2015,” [Online]. Available: http://www.trinasolar.com/HtmlData/downloads/us/Annual_report_of_Laboratory_PV_ST_EN.pdf. [Accessed September 2016].

[3] E. Skoplaki and J. Palyvos, "On the temperature dependence of photovoltaic module electrical perfromance: a review of efficiency/power correlations," *Solar Energy,* vol. 83, pp. 614-624, 2009.

[4] E. Sjerps-Koomen, E. Alsema and W. Turkenburg, "A simple model for PV module reflection losses under field conditions," *Solar Energy,* vol. 57 , no. 6, pp. 421-432, 1996.

[5] M. Duell, M. Ebert, M. Muller, B. Li, M. Koch, T. Christian, R. Perdichizzi, B. Marion, S. Kurtz and D. Doble, "Impact of structured glass on light transmission, temperature and power of PV modules," in *EUPVSEC*, Valencia, Spain, 2010.

[6] A. Nositschka, "Sun-Light Harvesting with Surface Patterned Glass for Photovoltaics," International Materials Institute for New Functionality in Glass, Pittsburgh, PA, USA, 2008.

[7] S. Krauter, "Betriebsmodell der optischen, thermischen und elektrischen Parametern von PV-Modulen". PhD Thesis,Technischen Universität Berlin 1993.

[8] M. Green, Solar Cells: Operating Principles, Technology and System Applications, Englewood Cliffs, NJ: Prentice-Hall, Inc., 1982.

[9] J. Zhou, Q. Yi, Y. Wang and Z. Ye, "Temperature distribution of photovoltaic module based on finite

element simulation," *Optoelectronics Letters,* vol. 111, pp. 97-103, 2015.

[10] M. Usama Siddiqui, A. Arif, L. Kelly and S. Dubowsky, "Three-dimensional thermal modeling of a photovoltaic module under varying conditions," *Solar Energy,* vol. 86, pp. 2620-2631, 2012.

[11] Y. Lee and A. Tay, "Finite Element Thermal Analysis of a Solar Photovoltaice Module," *Energy Procedia,* vol. 15, pp. 413-420, 2012.

[12] G. Johnston, "Focal region measurements of the 20 m2 tiled dish at the Australian National University," *Solar Energy,* vol. 63, no. 2, pp. 117-124, 1998.

[13] V. Quaschning, Understanding renewable energy systems, vol. 1, London: Earthscan/Routledge, 2005.

[14] M. Wolf and H. Rauschenbach, "Series resistance effects on solar cell," *Advanced Energy Conversion,* vol. 3, pp. 455-479, 1963.

[15] H. Wirth and C. Ferrara, "PV Module Technology and Reliability – Status and Perspectives," *Green,* vol. 2, no. 4, pp. 159-169, 2012.

[16] M. G. Villalva, J. R. Grazoli and E. R. Filho, "Comprehensive Approach to modeling and simulation of PV arrays," *IEEE Transactions on Power Electronics,* vol. 24, no. 5, pp. 1198-1208, 2009.

[17] H. A. Zondag, "Flat-plate PV-Thermal collectors and systems: A review," *Renewable & Sustainable Energy Reviews,* vol. 12, pp. 891-959, 2008.

[18] D. Evans, "Simplified method for predicting photovoltaic array output," *Solar Energy,* vol. 27, no. 6, pp. 555-560, 1981.

[19] K.-J. Bathe, Finite Element Procedures, Englewood Cliffs, NJ: Prentice Hall, 1996.

[20] O. C. Zienkiewicz, The finite element method, vol. 3, London: McGraw-Hill, 1977.

[21] B. E. A. Saleh and M. C. Teich, Fundamentals of Photonics, New York: Wiley, 1991.

[22] M. Born and E. Wolf, Principles of Optics, vol. Seventh, Cambridge: University Press, 2003.

[23] J. Duffie and W. A. Beckman, Solar Engineering of Thermal Processes, vol. 3, New Jersey: Wiley, 2006.

[24] G. Notton, C. Cristofari, M. Mattei and P. Poggi, "Modelling of a double-glass photovoltaic module using finite differences," *Applied Thermal Engineering,* vol. 25, pp. 2854-2877, 2005.

[25] E. Franklin and J. Coventry, "Effects of highly non-uniform illumination distribution on electrical performance of solar cells," in *Proceedings of Australia & New Zealand Solar Society*, Canberra, 2002.

[26] A. Mette, "New concepts for front side metallization of industrial solar cells". PhD thesis, Universität Freiburg 2007.

[27] A. Haas, J. Wilcox, J. Gray and R. J. Schwartz, "Numerical modeling of loss mechanisms resulting from non-uniform illumination in multijunction concentrator solar cells," *International Journal of*

Numerical Modelling: Electronic Networks, Devices and Fields, vol. 27, pp. 282-297, 2014.

[28] G. Smirnov and J. Mahan, "Distributed series resistance in photovoltaic devices: intensity and loading effects," *Solid-State Electronics,* vol. 23, no. 10, pp. 1055-1058, 1980.

[29] K. Mitchell, "Computer analysis of resistance and non-uniform illumination effects on concentrator solar cells," in *International Electron Devices Meeting*, Sandia hboratories, AlbuquerqueN,M 87115, 1977.

[30] M. Green and M. Keevers, "Optical properties of intrinsic silicon at 300 K," *Progress in Photovoltaics,* vol. 3, no. 3, pp. 189-192, 1995.

[31] "Solar cell central," 2011. [Online]. Available: http://solarcellcentral.com/images/silicon_absorption.jpg. [Accessed September 2016].

[32] M. Rubin, "Optical Properties of Soda-Lime Silica Glasses," *Solar Energy Materials,* vol. 12, no. 4, pp. 275-288, 1985.

[33] S. Krauter, Betriebsmodell der optischen, thermischen und elektrischen Parametern von PV-Modulen, Berlin: Köster, 1993.

[34] T. Fellmeth, F. Clement and D. Biro, "Analytical Modeling of Industrial-Related Silicon Solar Cells," *IEEE Journal of Photovoltaics,* vol. 4, no. 1, pp. 504-513, 2014.

[35] J. K. Kim H., E. Lee, D.-W. Kim, J.-H. Yun and J. Yi, "Effect of the short collection length in silicon microscale wire solar cells," *Applied Physics Letters,* vol. 102, no. 19, 2013.

[36] J. Coventry, "Performance of a concentrating photovoltaic/thermal collector," *Solar Energy,* vol. 78, pp. 211-222, 2005.

[37] "VarioCAM Operating Instructions," January 2007. [Online]. Available: http://www.infratec.de/fileadmin/media/IRMT/Handbuecher/InfraTec-Manual-VarioCAM.pdf. [Accessed September 2016].

[38] T. Schott, "Operational Temperatures of PV modules," in *Proc. 6th European Photovoltaic Solar Energy Conference*, London, UK, 1985.

[39] K. McIntosh, J. Cotsell, J. Cumpston, A. Norris, N. Powell and B. Ketola, "An optical comparison of silicone and EVA encapsulants for conventional silicon PV modules: A ray-tracing study," in *34th IEEE Photovoltaic Specialists Conference*, Philadelphia, 2009.

[40] "DuPont Tedlar PVF General properties," 2014. [Online]. Available: http://www.dupont.com/content/dam/dupont/products-and-services/membranes-and-films/pvf-films/documents/DEC_Tedlar_GeneralProperties.pdf. [Accessed September 2016].

[41] R. French, J. Rodriguez-Parada, M. Yang, R. Derryberry and N. Pfeiffenberger, "Optical Properties of polymeric materials for concentrator photovoltaic systems," *Solar Energy Materials & Solar Cells,* vol. 95, pp. 2077-2086, 2011.